

Myeloid lineage C3 induces reactive gliosis and neuronal stress during CNS inflammation

Received: 4 August 2024

Accepted: 25 March 2025

Published online: 12 April 2025

 Check for updates

Thomas Garton ^{1,8}, Matthew D. Smith ^{1,8}, Ajay Kesharwani ¹,
Marjan Gharagozloo ¹, Sungtaek Oh ^{1,2}, Chan-Hyun Na ^{1,2},
Martina Absinta ^{1,3,4,5}, Daniel S. Reich ^{1,3}, Donald J. Zack ^{6,7} &
Peter A. Calabresi ^{1,6,7} ✉

Complement component C3 mediates pathology in CNS neurodegenerative diseases. Here we use scRNAseq of sorted C3-reporter positive cells from mouse brain and optic nerve to characterize C3 producing glia in experimental autoimmune encephalomyelitis (EAE), a model in which peripheral immune cells infiltrate the CNS, causing reactive gliosis and neuro-axonal pathology. We find that C3 expression in the early inflammatory stage of EAE defines disease-associated glial subtypes characterized by increased expression of genes associated with mTOR activation and cell metabolism. This pro-inflammatory subtype is abrogated with genetic C3 depletion, a finding confirmed with proteomic analyses. In addition, early optic nerve axonal injury and retinal ganglion cell oxidative stress, but not loss of post-synaptic density protein 95, are ameliorated by selective deletion of C3 in myeloid cells. These data suggest that in addition to C3b opsonization of post synaptic proteins leading to neuronal demise, C3 activation is a contributor to reactive glia in the optic nerve.

Neurodegenerative diseases are increasingly prevalent with our aging population and are largely untreatable. When neurons die in the CNS there is a robust astroglial and microglial response characterized by phagocytosis and clearance of cellular debris, which may facilitate tissue repair^{1,2}. However, both of these glial types also have effector functions that are deleterious. They can recruit peripheral immune cells and release injurious molecules, including cytokines and factors associated with oxidative stress³. The early complement component C3 is one of the most highly differentially expressed genes in neurotoxic astroglia, is elevated in most neurodegenerative diseases, and is specifically associated with multiple sclerosis (MS) disease severity^{4,5}.

Genetic deletion of C3 in the murine experimental autoimmune encephalomyelitis (EAE) models of MS is protective of synapses in the hippocampus and lateral geniculate nucleus, supporting the notion that C3-mediated pathology is a major mechanism of injury^{6,7}.

The mechanisms by which the prominent neuroinflammation observed in MS progresses into neurodegeneration are still not fully understood. The inability of lymphocyte-modifying therapies to arrest the progressive form of the disease has highlighted the key role that glial cells play in initiating and sustaining smoldering neuroinflammation⁸. Indeed, astro and microglial cells may be primary drivers of neuronal loss both in MS and in other

¹Department of Neurology, Johns Hopkins University School of Medicine, Baltimore, MD 21287, USA. ²Institute for Cell Engineering, Johns Hopkins University, Baltimore, MD 21205, USA. ³Translational Neuroradiology Section, National Institute of Neurological Disorders and Stroke (NINDS), National Institutes of Health (NIH), Bethesda, MD, USA. ⁴Department of Biomedical Sciences, Humanitas University, Milan, Italy. ⁵IRCCS Humanitas Research Hospital, Milan, Italy. ⁶Department of Ophthalmology, Wilmer Eye Institute, Johns Hopkins University School of Medicine, Baltimore, MD 21287, USA. ⁷Solomon H. Snyder Department of Neuroscience, Johns Hopkins University, Baltimore, MD 21205, USA. ⁸These authors contributed equally: Thomas Garton, Matthew D. Smith.

✉ e-mail: pcalabr1@jhmi.edu

neurodegenerative diseases^{9–11}. Since optic neuritis and retinal pathology are hallmarks of MS¹², and given the retina's accessibility to noninvasive monitoring with techniques such as optical coherence tomography (OCT), the anterior visual pathway (AVP) provides an attractive neuroanatomical location to study how CNS-localized cells contribute to neuroinflammation and subsequent neurodegeneration.

In a recent study, we observed the loss of retinal ganglion cells (RGCs) in post-mortem retinas from people with MS (pwMS) and identified elevated levels of complement component C3 in reactive astroglial regions of retinas that had thinning on OCTs obtained in vivo¹³. Complement fulfills physiological roles in the retina: early complement components C1q and C3 have been shown to be involved in retinal synaptic pruning during normal development^{14,15}. C3 can bind to cellular surfaces following its activation by C3 convertases into C3b, at which point it serves as a target for microglia and macrophages that express the C3 receptor (CD11b). These phagocytic myeloid cells then eliminate excess synapses opsonized in this manner to facilitate somatotopic projections^{3,16}. While complement has therefore been shown to be important in the CNS during development through its ability to opsonize synapses, C3 has also been implicated in contributing to inflammatory environments during disease, with CNS-resident cell types such as astrocytes and microglia being noted as significant sources of early complement components^{4,17}. Furthermore, C3 is expressed highly even in the synapse-free white matter, such as in chronic active MS lesions in both microglia inflamed in MS (MIMS)¹⁰ and in reactive astrocytes across multiple neurodegenerative diseases^{18,19}. Co-localization of elevated levels of C3 onto synapses during inflammation has led to the hypothesis that elevated complement may be aberrantly opsonizing synapses^{7,20,21}, leading to excessive synaptic damage and subsequent neuronal death. Early excessive synaptic loss leading to neurodegeneration is also reported in other diseases such as Alzheimer's^{22,23}, Huntington's²⁴, and West Nile virus²⁵, making the hypothesis relevant to the broader question of neurodegenerative mechanisms. However, it has been shown that synaptic pruning or reduction in synaptic signaling can also be a protective response by neurons that are experiencing stress and injury to temporarily reduce excitatory input^{26,27}. In this situation, where the injury is not due to excessive synaptic stripping, C3 may still be an important contributor to the activation of glia in the optic nerve using similar mechanisms as those that occur in the periphery. In addition to the role of circulating complement as an opsonin, C3 is also known to be activated by proteases or C3 convertases to form C3a in the extracellular space where it can act in a paracrine or autocrine manner by binding to complement receptors such as C3aR1. Many of these complement receptors are expressed on astrocytes, microglia, and a subset of classical CD16⁺ monocytes which are involved in CNS immune surveillance and inflammation^{28–30}. Furthermore, there are several examples of C3a having intracellular functions as part of what is now called the complosome. In such instances, C3a can signal intracellularly in adaptive and innate immune cells and modulate immune cell metabolism, autophagy, and gene regulation³¹. Complosome activity has also been described recently in synovial fibroblasts where intracellular C3a-C3aR activity led to increased mammalian target of rapamycin (mTOR) activity, a pathway strongly linked with both cellular survival and inflammation³². Another possibility is that C3's inflammatory effects might be mediated by downstream complement activation, as C3 forms a component of the C5 convertase that eventually leads to the formation of the membrane attack complex (MAC). However, previous studies have shown that mice deficient in C5 (which therefore are unable to produce the MAC) actually experienced worsened demyelination and axonal damage in EAE^{33,34}, suggesting that the majority of the detrimental actions of complement stem from early complement components such as C3.

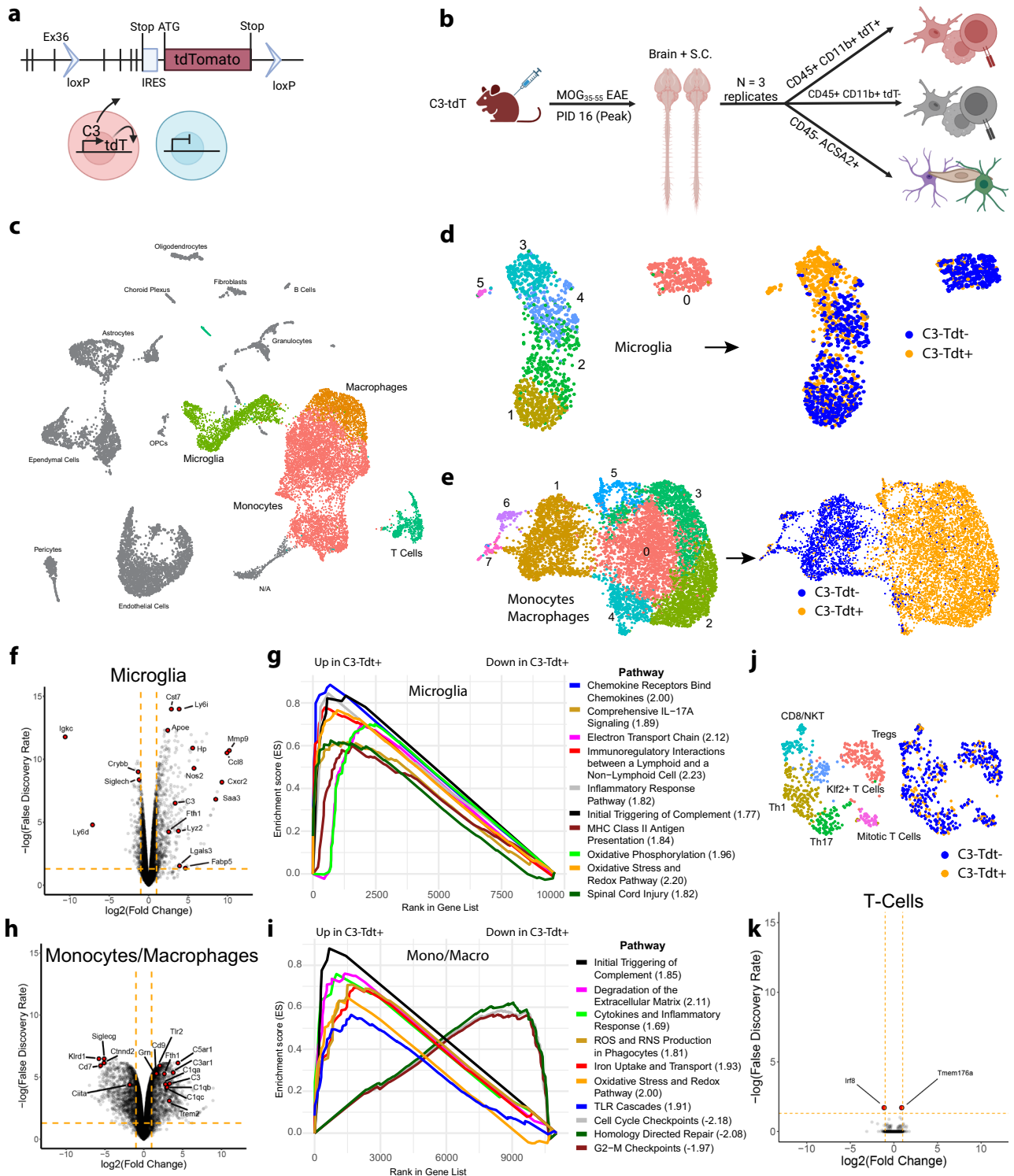
During EAE, mice injected with immunogenic myelin peptides reliably develop inflammation, optic neuritis, and eventually loss of RGCs³⁵. Astrocytes and microglia are activated in the retina as well as the optic nerve early in the course of disease³⁶. Global and astrocyte-specific deletion of the C3 gene results in amelioration of RGC loss and promotes neurite health in the EAE retina¹³. However, other models of CNS injury have highlighted microglia and other myeloid cells as having the potential to dramatically upregulate C3 production^{37,38}. Additionally, given C3's cleavage products' ability to signal via complement receptors and modulate immune and CNS cell profiles, studying whether C3 may play a role bridging the gap between inflammation and neurodegeneration beyond opsonization is worth considering. C3 has been suggested to be important for mediating inflammatory glial crosstalk³⁹, yet the effect of C3 depletion on cellular phenotype and transcriptomic profiles has not been examined in EAE.

In this work, we leverage a floxed C3-tdTomato reporter mouse line to characterize CNS cells which produce C3 during neuroinflammation, how C3 depletion would affect the transcriptomic landscape of the AVP, and whether we could identify early signs of C3-mediated pathology in the retina of EAE mice.

Results

Single cell analysis of EAE CNS tissue demonstrates C3-defined myeloid cells

Both astroglia and CNS myeloid cells (including resident microglia and infiltrating monocytes) are known to upregulate C3 following adaptive immune-mediated inflammation and aging^{13,37,38}. We therefore sought to use single cell transcriptomics to characterize both myeloid and non-myeloid C3 producing cells in the CNS during inflammation. We induced EAE in six transgenic C3-tdTomato reporter mice, a previously described mouse line that allowed us to identify C3 producing cells using a fluorescent reporter and sort them without fixation⁴⁰. We waited 18 days after immunization (~2–4 days after disease score peak) to collect the tissue to allow ample time for peripheral monocyte recruitment and activation as well as local astrocyte and microglial response. We dissociated brain and spinal cord from the six transgenic mice and created 3 independent pooled samples (2 mice per pool), then labeled and sorted cells from each pool into three populations: C3 positive myeloid cells (CD45⁺;CD11b⁺;C3 reporter positive), C3 negative myeloid cells (CD45⁺;CD11b⁺;C3 reporter negative), and a third population that included both C3 positive and negative astrocyte cell surface antigen 2 (ACSA2)⁺ cells (CD45⁺;ACSA2⁺;C3 reporter positive and negative) (Figs. 1a, b, S1a). Surprisingly, we detected very few C3-reporter positive ACSA2⁺ cells (Supplemental Fig. S1b, c) which suggests these cells are not efficiently isolated with this procedure. Given how few of the ACSA2⁺;C3⁺ cells we observed, we gated this third population in such a way to enrich for the C3⁺ population while still capturing C3⁻ cells as well to ensure that the few ACSA2⁺;C3⁺ cells sorted would not be lost in subsequent washing steps due to low initial yield (Supplemental Fig. S1b). In total we generated 9 samples - 3 cell types from 3 replicates (Supplemental Data 1). We then performed single cell transcriptomics using a commercial probe-based assay⁴¹ targeting 19,070 genes that allowed us to multiplex the 9 samples using equal numbers of cells from each sample into a single library while retaining which sample each cell originated from. An added advantage of this strategy is that, by sorting the C3 positive and negative cells separately in the myeloid population, we could identify which population each cell came from without relying on detection of the C3 transcript itself in the transcriptomic data. We captured 17,133 cells across 9 samples which we merged into a single dataset. The combined dataset contained 13 distinct cell types over 28 different clusters (Figs. 1c; S2, Supplemental Data 2). We then subsetted the microglia clusters (identified by expression of *P2ry12*, *Tmem119*, and *Sparc*) and monocyte/macrophage clusters (identified by expression of *Clec12a* and *Ccr2* (Fig. S2f) separately^{42,43}. The microglia



subclustering revealed 6 subclusters, with clusters 0, 1, 2, and 4 consisting primarily of cells from the C3-tdTomato⁻ sorted populations, while clusters 3 and 5 contained cells primarily from the C3-tdTomato⁺ sorted population (Fig. 1d). Amongst the C3⁻ clusters, cluster 1 contained the highest levels of classic homeostatic markers *P2ry12*, *Tmem119*, and *Fcrls*, while cluster 4 was positive for interferon-responsive genes (*Ifitm10*, *Ifitm3*) and MHC-II antigen presentation genes (*Cd74*, *H2-Aa*, *H2-Eb1*), together indicating the existence of both homeostatic and pro-inflammatory C3⁻ populations (Fig. S3). Similarly, monocytes/macrophages were segregated into two major populations defined by production of C3, suggesting a significant difference

between C3⁺ and C3⁻ myeloid cells (Fig. 1e). Indeed, differential gene expression analysis comparing C3⁺ and C3⁻ sorted samples indicated 3533 differentially expressed genes (DEGs) in microglia, with inflammation-linked genes such as *Apoe*, *Saa3*, *Fth1*, and *Lyz2* being upregulated in C3⁺ microglia, while more homeostatic genes such as *Crybb* and *Siglech* were downregulated (Fig. 1f). Gene set enrichment analysis (GSEA) of these microglial DEGs showed enrichment for IL-17 and T cell signaling in C3⁺ microglia, as well as antigen presentation and metabolic processes like oxidative phosphorylation (Fig. 1g) among others. C3⁺ monocytes and macrophages broadly upregulated early complement cascade proteins and their receptors (*C1qa*, *C1qb*,

Fig. 1 | Single cell RNA-sequencing of C3-tdTomato mice reveals that myeloid cells have distinct populations defined by expression of C3 in the setting of EAE. **a** Schematic of the C3-tdTomato reporter, showing the insertion of an IRES site and reporter gene following the final C3 exon, with flanking loxP sites allowing for excision by a Cre recombinase. As a nonfusion reporter, the tdTomato remains intracellular following expression allowing for identification of C3-producing cells. **b** Experimental paradigm. EAE was induced in 6 mice allowing for 3 independent replicates of 2 pooled brains and spinal cords each. For each replicate, sorting was performed on CD45, CD11b, ACSA2, and tdTomato to collect tdTomato⁺ and tdTomato⁻ myeloid cells, and an astrocyte-enriched third sample. **c** UMAP plot of integrated dataset with key populations (from the CD45⁺ sorted samples) colored while the CD45⁻ ACSA2⁺ sample is in grey. Each cluster is annotated with cell identity (the cluster labeled N/A was not able to be identified). **d, e** Hierarchical subclustering and reanalysis of microglia and monocytes/macrophages separately

with the tdTomato⁺ sample highlighted in orange and the tdTomato⁻ sample highlighted in blue. **f**, Volcano plot showing DEGs in microglia based on tdTomato expression. A positive log fold change represents genes upregulated in tdTomato⁺ microglia. Dashed yellow lines represent FDR of 0.05 (horizontal) and log2FC of +/−1 (vertical lines). **g**, GSEA indicating directionality of pathways in C3-tdTomato⁺ microglia compared to C3-tdTomato⁻ microglia. Normalized enrichment scores indicated in parentheses. **h** as in (f) but for C3-tdTomato⁺ monocytes/macrophages. **i** as in (g) but for monocytes/macrophages. **j**, UMAP plot of the captured T cells showing diverse subtypes with cells from the tdTomato⁺ sort in orange, cells from the tdTomato⁻ CD11b⁺ sort in blue, and cells from the ACSA2⁺ sort in grey. **k** Volcano plot of DEGs in T cells based on C3-tdTomato expression. Figure 1a created in BioRender. Smith, M. (2025) <https://BioRender.com/w65n506>. Figure 1b created in BioRender. Smith, M. (2025) <https://BioRender.com/e30b984>.

C1qc, *C3ar1*, *C5ar1*) when compared to C3⁻ monocytes and macrophages (Fig. 1h) as did microglia, although to a lesser extent. As with microglia, inflammatory cytokine production was upregulated in C3⁺ monocytes/macrophages, while pathways associated with cell cycle progression and DNA repair (for example, *Kntc1*, *Cenpm*, *Exo1*, *Cdc7*) were suppressed (Fig. 1i). We confirmed the presence of these C3⁺ myeloid subclusters in a second single cell transcriptomic experiment, this time using 3′ RNA sequencing instead of probe-based (Fig. S4). Given the lossy and multiplet-prone nature of massively parallel single cell transcriptomic experiments, it remains possible that there is cross-contamination between the microglia and monocyte/macrophage subsets detected. We observe, however, a great deal of overlap between C3⁺ microglia and C3⁺ monocytes/macrophages when compared to their respective C3⁻ populations (complement cascade, oxidative stress and redox pathway, cytokine and chemokine signaling) suggesting that similar pathways are at work in both populations which would render modest cross-contamination less problematic.

Two additional C3⁺ clusters (identified based on presence of C3 transcript) were noted in the CD45⁺;ACSA2⁺ sorted population, belonging to a subset of ependymal cells that also upregulated antigen presentation, phagocytosis, IL-17 signaling, and pro-inflammatory cytokines (Fig. S5) and a reactive astrocyte cluster that upregulated T cell interactions but downregulated cholesterol and fatty acyl biosynthesis (Fig. S6). We further confirmed the presence of this C3⁺ reactive astrocyte cluster in an independent previously-published 3′ RNA sequencing dataset⁴⁴ and confirmed that C3-producing astrocytes contained the highest levels of classic reactive astrocyte markers, upregulated inflammatory signaling pathways, and downregulated the IL-10 signaling pathway (Fig. S7). Despite not directly sorting for lymphocytes, we did still capture a cluster of contaminating T cells that contained a wide spectrum of polarizations, including Th1 cells, Th17 cells, Tregs, CD8⁺ cells, and NKT cells. However, unlike the myeloid cell clusters, C3⁺ T cells did not cluster independently from the C3⁻ lymphocytes (Fig. 1j). Differential expression analysis indicated that there were only two DEGs between C3⁺ and C3⁻ T cells, suggesting that unlike in microglia and monocytes/macrophages, C3 production is not a defining feature of CNS T cells in this murine model of neuroinflammation (Fig. 1k).

C3⁺ microglia in EAE resemble Microglia Inflamed in MS (MIMS)

A recently-identified microglial subtype defined by early classical complement production called MIMS is highly correlated with pathology around paramagnetic rim chronic active white matter lesions in MS and express elevated levels of C3¹⁰. We were therefore curious whether the C3⁺ microglia we observed in EAE were transcriptionally similar to these MIMS. We first compared the expression of the 16 MIMS marker genes¹⁰ in C3-tdTomato⁺ microglia to their non-C3 producing counterparts and found that 14/16 of those genes were significantly upregulated in the C3⁺ cells (FDR < 0.05, Fig. 2a). These MIMS markers were only associated with cluster 3 microglia.

The other C3⁺ microglial cluster, cluster 5 did not show elevated expression of any of the classic MIMS markers (Fig. 2b). Comparing cluster 3 to the other microglia showed that cluster 3 was characterized primarily by not only the MIMS markers and antigen presentation, but by *Saa3* (recently shown to be involved in maintenance of Th17 cells in the CNS following inflammation⁴⁵), *Fabp5* (a potentially pathologic modulator of the immune response in EAE⁴⁶), and *Spp1* (recently shown to be critical in the ability for microglia to phagocytose synapses in a model of Alzheimer’s Disease⁴⁶) (Fig. 2c). Cluster 3 microglia broadly upregulated genes associated with metabolic processes including the electron transport chain, glycolysis and gluconeogenesis, as well as translation (Fig. 2d). In contrast, cluster 5 microglia were defined by production of the calcium binding proteins *S100a8* and *S100a9*, which are involved in leukocyte recruitment⁴⁷, as well as IL-1 signaling genes and *Mmp9* (Fig. 2c). GSEA on cluster 5 microglia in comparison to all other microglial subtypes showed upregulation of chemokine-chemokine receptor interaction pathways and interferon signaling, with a stronger focus on signaling to lymphocytes (Fig. 2e). In the initial characterization of MIMS derived from post-mortem samples of pwMS, two sub-populations were observed – MIMS-foamy and MIMS-iron. The foamy subtype had elevated expression of genes related to lipid storage, response to lipoprotein particles and inflammatory regulation. The other population, MIMS-iron, was notable for expression of genes related to ferritin complex, MHC Class II, and ribosomal genes. We did not observe enrichment for genes from one type or the other in the C3⁺ microglia analyzed, instead we saw expression of both (ie lipid storage and response – *Lpl*, *ApoE* as well as ferritin complex – *Fth1*) (Fig. 2a, b). This discrepancy may be a result of low cell count (microglia cluster 3 is 236 cells which may not be enough to resolve two distinct phenotypes) or differences between the animal model and human disease (particularly that EAE is an acute condition vs the chronic time point at which human tissue is collected). Together, these analyses demonstrate the presence of two distinct C3⁺ microglial cell clusters in EAE, one characterized by the presence of MIMS genes and metabolic demand and the other by immune cell interactions.

Global C3 depletion affects astrocyte and myeloid transcriptomes and results in dramatic reduction of pro-inflammatory phenotypes

Given the pro-inflammatory characteristics of the cells defined by C3 production, we hypothesized that C3 deletion might attenuate their potentially pathological transcriptomes. We chose to test this hypothesis by performing snRNA-seq analysis on unsorted nuclei from the optic nerves of mice 16 days after EAE immunization, based on our recent findings of the role for C3 in mediating RGC loss and AVP pathology¹³. Due to the challenge posed by the small tissue size of each optic nerve, we pooled optic nerves from 5 EAE mice (10 optic nerves total) per sample and compared two C3KO samples to two WT samples

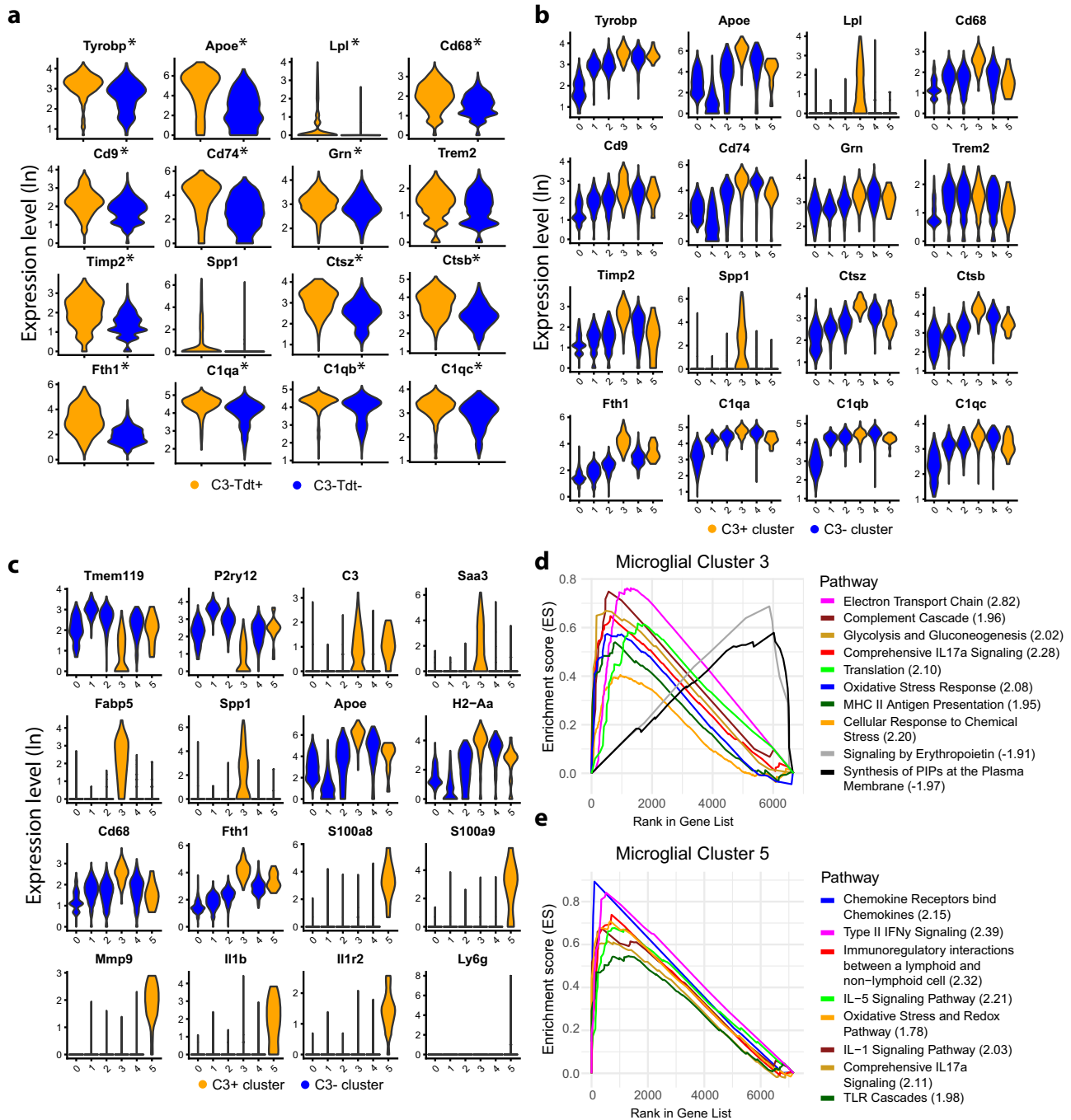


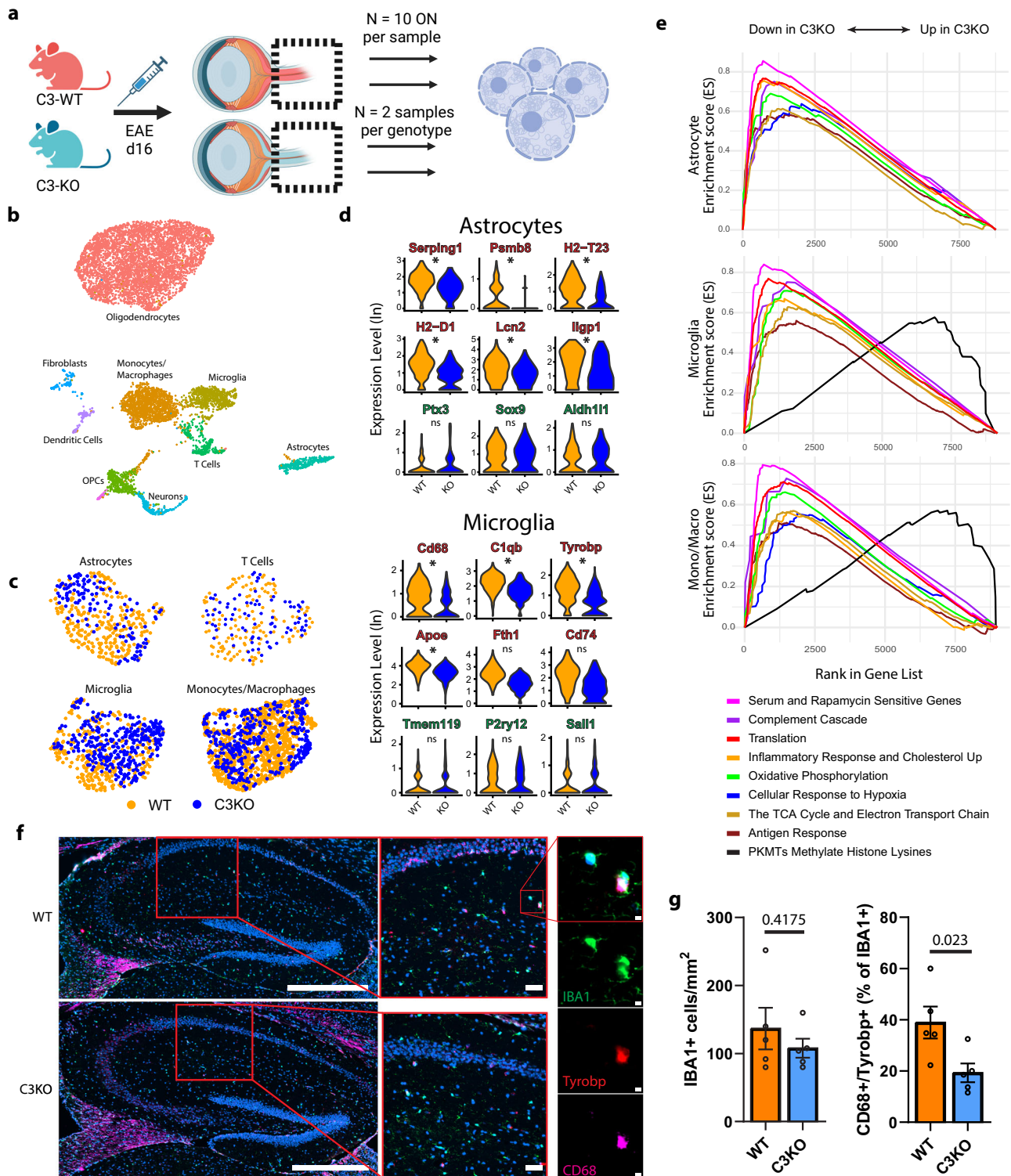
Fig. 2 | EAE mice harbor two distinct C3+ microglial populations including a MIMS-like phenotype that is enriched in lysosomal clearance pathways. **a** Violin graphs showing expression of 16 MIMS markers in C3-tdTomato⁺ (orange) and C3-tdTomato⁻ (blue) microglia. *N* = 3 samples. Asterisks next to the gene name denotes that comparison has FDR < 0.05. FDR value derived from pseudobulk differential expression test with edgeR. **b** Violin graphs showing the 16 canonical MIMS markers

broken down over each microglial subcluster. Orange clusters are the two C3⁺ tdTomato⁺ clusters. **c** Panel of selected markers for cluster 3 and cluster 5. **d, e** GSEA indicating directionality of pathways in cluster 3 and 5 respectively. Pathways that peak on the left are upregulated in that cluster. Normalized Enrichment Score is included in parentheses after the pathway name.

(Figs. 3a; S8). We have previously shown that in our experience, global C3KO animals are not protected from EAE induced paralysis and that there is no difference in the immune infiltrate (including T-cell polarization and peripheral myeloid cell recruitment) between WT and C3KO animals at the peak of disease¹³. To further control for possible effects of C3 depletion on adaptive immune infiltrate, we matched samples based on EAE disease score (Supplemental Data 1).

Our experiment yielded 9,412 nuclei across the four samples, which included oligodendrocytes, astrocytes, microglia, monocytes/

macrophages, and T cells as well as other populations such as OPCs, dendritic cells, fibroblasts, and vascular endothelium across 17 clusters (Figs. 3b; S8). We then subsetted individual cell types and repeated dimensionality reduction, after which we observed that while C3KO and WT cells did not completely separate in the reduced dimension space, they did appear to segregate within the astrocytes, microglia, and monocytes/macrophage cell types (Fig. 3c) indicating some distinction between the C3KO and WT cells. We further explored this separation by genotype in the microglia by performing



clustering and differential abundance analyses. Seven clusters were identified in the subsetted microglia and while they showed some overlap, distinct expression patterns did exist (Fig. S9a). Cluster 0 had the highest expression of homeostatic microglia genes such as *P2ry12* and *Csf1r* which are known to be suppressed upon activation and suggests that cluster 0 represents a less activated subset of microglia. Cluster 2 on the other hand had the highest expression of a variety of genes previously identified as enriched in MIMS including *Tyrobp*, *Apoe*, *C1qa*, and *Fth1* in addition to genes related to translation suggesting a highly activated subset. Differential abundance

analyses showed that the WT microglia were enriched in cluster 2 while the KO microglia were enriched in cluster 0 (Fig. S9b). Even within the same cluster, wild type nuclei showed lower expression of homeostatic genes (cluster 0) and higher expression of reactive genes (cluster 2) (Fig. S9c, d). Other clusters also showed evidence of a distinct reactive state, such as clusters 1 and 3 which had higher expression of genes related to lipid transport and metabolism (*Abca1*, *Eepd1*, *Acs1l*, *Lpl*) and cluster 5 which had high expression of canonical interferon response genes such as *Ilgp1*, *Cxcl10*, *Oas3*, and *Stat1* (Supplemental Data 3).

Fig. 3 | Single nucleus RNA-sequencing from optic nerves reveals that global C3 depletion results in widespread alterations in transcription characterized by a reduction in reactive glial profiles. **a** Experimental paradigm. 10 C3KO mice and 10 WT mice were immunized and carried out to the peak of disease (PID 16). 5 mice were pooled per sample, resulting in 10 optic nerves per sample that were flash frozen and from which nuclei were extracted. snRNA-seq analysis was performed on the resulting 4 samples. **b** Annotated integrated UMAP plot of nuclei captured from optic nerves of $N = 2$ WT samples and $N = 2$ C3KO samples (See Fig. S8 for full UMAP and cluster identification markers). **c** Hierarchical subclustering and reanalysis of four key cell types showing cells from WT samples in orange and cells from C3KO samples in blue. **d** Specific gene changes in astrocytes and microglia. Gene names in red indicate MIMS and TIC-responsive genes in microglia and astrocytes respectively. Green gene names indicate homeostatic or neuroprotective genes. $FDR < 0.1$ denoted with an asterisk. **e** GSEA of DEGs in C3KO vs WT astrocytes (top),

microglia (middle), and monocytes/macrophages (bottom). Color scheme for each pathway indicated below the GSEA plots. Pathways with peaks on the left are downregulated in C3KO cells. All shown pathways have $FDR < 0.05$.

f Representative image of immunofluorescent staining of hippocampi from the mice used for the optic nerve snRNA-seq experiment (top is WT, bottom is C3KO). CA-1 region used for quantification highlighted. Inset depicts an example of an IBA1⁺ CD68⁺ Tyrobp⁺ cell from a WT mouse: Scale bar = 500 μ M in low magnification view of hippocampus, 50 μ M in high magnification insets, and 5 μ M in single cell magnification insets. **g** Quantification of IBA1⁺ CD68⁺ Tyrobp⁺ cells in the CA-1 region of the hippocampus ($N = 5$ mice per genotype, WT average final EAE score = 2.3 ± 0.24 ; C3KO average final EAE score = 1.9 ± 0.2 ; 60% male in both genotypes; p -value from unpaired student t -test, data presented as mean \pm SEM). Source data are provided as a source data file. Figure 3a created in BioRender. Smith, M. (2025) <https://BioRender.com/k30u268>.

Differential expression testing comparing C3KO and WT astrocytes, microglia, and monocytes/macrophages using pseudobulked data identified numerous DEGs with $FDR < 0.05$ in multiple cell types (156 DEGs in astrocytes, 102 in monocytes/macrophages, and 163 in microglia) (Fig. S9). Notably, oligodendrocytes were more modestly affected (Fig. S10), and in agreement with our first single cell transcriptomic experiment, T cells had no DEGs between the two conditions (Fig. S11). C3KO astrocytes exhibited specific reduction in expression of TNF, IL1a, and C1q-induced (TIC) genes *H2-D1*, *H2-T23*, *Psmb8*, *ligp1*, and *Serping1*⁷ as well as the pan-reactive marker *Lcn2* while not affecting the ischemia-specific *Ptx3* or the homeostatic markers *Sox9* and *Aldh1l1* (Fig. 3d). Critically, we confirmed that C3KO significantly decreased the presence of MIMS markers in microglia such as *Cd68*, *C1qb*, *Tyrobp*, and *ApoE*, with similar trends in *Fth1* and *Cd74*, while the expression of homeostatic microglial markers *Tmem119*, *P2ry12*, and *Sall1* were unchanged in the C3KO samples (Fig. 3d). GSEA showed a common theme across astrocytes, microglia, and monocytes/macrophages, with mTOR signaling, complement cascade, translation, oxidative phosphorylation, inflammatory response, and antigen presentation all being significantly downregulated in the C3KO compared to WT cells (Fig. 3e). We also identified downregulation of genes encoding ribosomal proteins in C3KO astrocytes, microglia, and monocytes/macrophages, consistent with a broad decrease in inflammatory hyperactivity and reductions in mTOR signaling, which regulates ribosomal biogenesis (Fig. S11)⁴⁸. Interestingly, very few pathways were upregulated in the C3KO samples, with methylation of histone lysines (a broad pathway with no singular downstream effect) being the sole pathway upregulated in microglia and monocytes/macrophages (Fig. 3e). There were many genes that were differentially expressed in only one cell type, implying cell-specific effects of C3 deletion (Fig. S12a). For example, *Tgfb3* was only upregulated in C3KO astrocytes, *Tnfr* was only downregulated in C3KO microglia, and *Trem2* was only downregulated in C3KO monocytes/macrophages. Conversely, there were a number of genes that were affected in all three of these key cell types, implying both cell-specific as well as more general changes in the setting of C3 deletion (Fig. S12b).

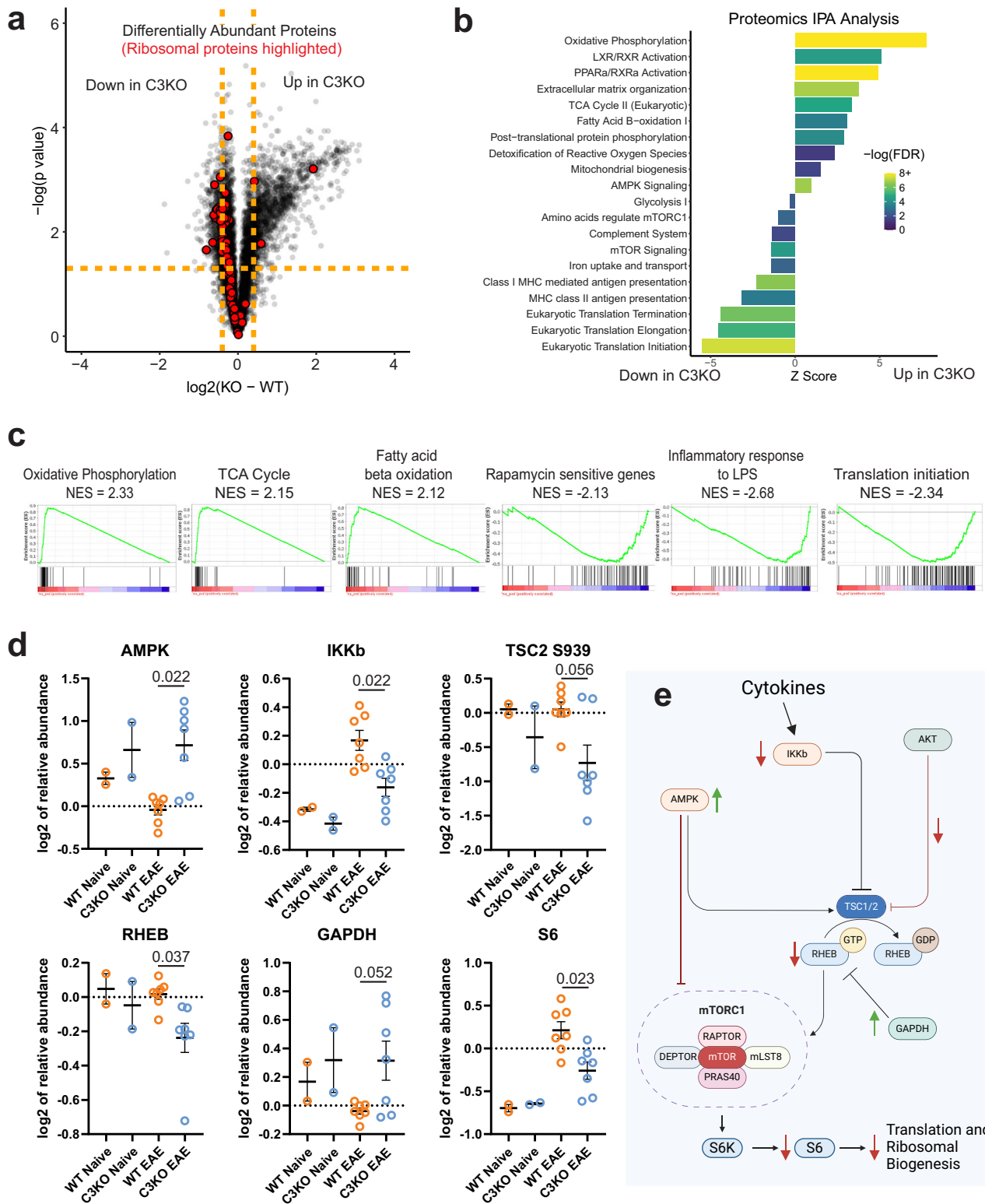
To assess whether this change in myeloid cell phenotype following C3 depletion was restricted to the optic nerve or present in other regions of the CNS, we used immunofluorescence staining to quantify CD68⁺TYROBP⁺ myeloid cells in the hippocampus. We chose these two markers as they are both genes previously shown to be upregulated in MIMS and were also differentially expressed in both our single cell transcriptomic studies (Figs. 2, 3). In addition, both are well described in the literature as markers of microglia and macrophage inflammation⁴⁹. We chose to look in the hippocampus because it is a grey matter region (as opposed to white matter of the optic nerve) that has previously been shown to have synapse loss in this model of EAE and is at least in part dependent on C3^{6,50,51}. As in the transcriptomic data from the optic nerve, we saw a decrease in CD68⁺;TYROBP⁺

double positive myeloid cells (IBA1⁺) in C3KO mice compared to WT controls with no change in overall myeloid cell density (Fig. 3f–g).

Given the depletion of pro-inflammatory phenotype in the microglia from C3KO animals compared to WT, we were curious whether the WT optic nerve microglia might more closely resemble the C3⁺ microglia in the brain and vice versa for the C3KO microglia and C3-microglia in the brain. We therefore integrated the optic nerve nuclei dataset with the sorted C3-tdTomato positive and negative microglia from the EAE brain (using the 3' poly-A dataset presented in Fig. S3 (Fig. S13c)). We observed 6 clusters in the integrated dataset and then tested for conserved marker genes shared between both datasets. Clusters 2, 3, and 5 had shared marker genes between both datasets and we focused on those (Fig. S13e, Supplemental Data 4). Cluster 2 had higher expression of several microglial identity genes suggesting a less reactive state, cluster 3 had higher levels of interferon response genes, and cluster 5 had the highest expression of C3, antigen presentation genes, and various other pro-inflammatory genes or MIMS related genes (Fig. S13g). When comparing the abundance of each sample (WT vs C3KO in optic nerve, C3-tdTomato⁺ vs C3-tdTomato-sorted in brain), we found that both C3WT optic nerve nuclei and C3-tdTomato⁺ sorted brain cells appeared to be enriched in the C3+ reactive cluster 5, while C3KO optic nerve nuclei and C3-tdTomato-sorted brain cells were enriched in the less activated cluster 2 (Fig. S13f). To determine whether these C3 depleted cells were returned to a “non-diseased” phenotype, we compared our single nuclei data with the single cell dataset from the recent paper by Fournier et al.⁵², which compared MOG-immunized animals to controls to elucidate differences between disease state and healthy brain. Integration of our dataset with theirs demonstrated that our C3KO microglia and astrocytes predominantly overlapped with their “control” cells, implying that C3KO restores microglia and astrocytes towards a healthy phenotype even in the setting of peak EAE (Fig. S13a, b). Our data therefore suggest that global C3 depletion has consistent effects on astrocyte and myeloid transcriptomes as well as cell-specific alterations, and that C3 depletion dramatically attenuates the disease-associated glial profiles and reduces metabolically demanding processes.

Proteomics reveals role of C3 in regulating mTORC1 at peak EAE

To explore whether these findings could be validated outside of transcriptomics, we performed a full proteomic and phosphoproteomic experiment on optic nerves of C3KO and WT mice at the peak of EAE. Specifically, we took 7 WT and 7 C3KO mice that were EAE score-matched as well as 2 naïve WT and 2 naïve C3KO mice to serve as non-disease controls, and we utilized mass spectrometry to evaluate relative protein and phosphorylation site abundance across all samples. While our lab has previously published that C3KO does not affect global inflammation in the EAE model¹³, we ensured our animals were matched in terms of their EAE scores to ensure that we were comparing animals that had similar inflammatory burden (EAE disease



score at day 16 reflects the amount of acute-stage inflammation in the spinal cord^{53,54}).

We observed that our C3KO mice did indeed have similar alterations in biological processes in our proteomics experiment as in our single cell transcriptomic experiments. Metabolic shifts away from inefficient glycolysis towards more energetically favorable oxidative phosphorylation in C3KO was confirmed and importantly, we observed agreement in the broad alterations in ribosomal biogenesis and mTORC1 signaling (Fig. 4a-c). By analyzing the upstream

regulators of mTORC1 activity, we identified a consistent effect of mTORC1 inhibition in our C3KO mice, which agrees with our transcriptomic studies and suggests a mechanism by which C3KO might be mediating its anti-inflammatory effects. mTORC1 is primarily regulated by RHEB which activates mTORC1 signaling⁵⁵. RHEB is decreased in C3KO (Fig. 4d), suggesting a reduced ability to activate mTORC1. This could be due to a trending increase in GAPDH which has been shown to bind to RHEB and cause its degradation. RHEB's activity is dependent on binding to GTP, and TSC1/2 act as GTPase-activating proteins

Fig. 4 | Proteomic and phosphoproteomic analysis of optic nerves at the peak of EAE to validate the effects of C3KO on mTORC1 signaling in the CNS.

a Volcano plot of all detected proteins in full proteomic analysis of $N = 7$ WT (mean score = 2) vs $N = 7$ C3KO (mean score = 1.8) EAE mouse optic nerves (each group consisted of mice from both sex). Both optic nerves from a mouse were needed to generate sufficient protein to constitute a biological replicate. To validate the findings of reduced ribosomal biogenesis in C3KO mice from our transcriptomic experiments (See supplemental Fig. S11) both small and large ribosomal proteins have been highlighted in red. **b** Ingenuity Pathway Analysis performed on the differentially abundant proteins from the proteomics experiment. Proteomics confirmed pathway-level decreases in mTOR signaling, glycolysis, mRNA translation, and antigen presentation in C3KO optic nerves, while C3KO mice upregulated energetically efficient processes like oxidative phosphorylation and the TCA cycle as well as reparative programs like the detoxification of reactive oxygen species. All pathways are significant by an adjusted p -value of <0.05 . **c** Pre-ranked GSEA was run

on the average relative log₂ fold change in protein abundances between EAE C3KO vs WT mice. Proteins that were most upregulated in C3KO mice lie on the left of the ranked protein list, so a positive Normalized Enrichment Score (NES) indicates an upregulated pathway in C3KO mice (scores listed above each plot). **d** Individual analysis of the abundance of proteins that regulate mTORC1 signaling. Adjusted p -values are listed as numbers above the comparison bars. Note that TSC2 S939 refers to relative abundance of phosphorylation of TSC2 at serine 939, a post-translational modification that inhibits the TSC complex from acting as a GAP for Rheb. All other bar graphs indicate total protein abundance. Note that we compared the 7 WT and 7 C3KO EAE mice to 2 WT and 2 C3KO naïve mice optic nerve proteomes for controls. Data presented as mean \pm SEM, one-way ANOVA adjusted for multiple comparisons. **e** Diagram depicting results from proteomics and phosphoproteomics experiments on how C3 knockout affects mTORC1 regulation. Figure 4e created in BioRender. Smith, M. (2025) <https://BioRender.com/d23a966>.

(GAPs) to swap out the GTP for GDP, thus inhibiting RHEB^{56,57}. The ability of TSC1/2 to do this depends on the activity of upstream kinases including AMPK (which activates TSC1/2⁵⁸ and is more abundant in C3KO), IKKb (which inhibits TSC1/2⁵⁹ and is less abundant in C3KO), and Akt (whose phosphorylation of TSC2 at S939 is known to inhibit TSC activity⁵⁹—the presence of this phosphorylation is reduced in C3KOs) (Fig. 4d). As evidence of a lack of mTORC1 activity there is a reduction in the amount of ribosomal protein S6 in C3KOs which is directly responsible for translation and ribosomal biogenesis⁶⁰ (Fig. 4d). Unlike the single cell resolution of the transcriptomic datasets, the proteomics were performed on full optic nerve which also includes neuronal axons, which raises the possibility that some of the alterations we observed are due to changes in neuronal proteomes. Many of the pathways we see differentially regulated between genotypes, however, are classically associated with glia. Additionally, given that we saw similar pathways across microglia, astroglia, and infiltrating monocytes/macrophages in our transcriptomic data (particularly mTOR signaling), seeing similar results from tissue level proteomics further supports this change following C3 depletion.

As in the transcriptomic analyses above, we once again performed immunofluorescent quantification in the hippocampus of WT and C3KO mice at peak EAE to assess whether the effect of C3 depletion in the optic nerve was present in other regions. Consistent with the optic nerve results, we found a decrease in the percentage of myeloid (IBA1+) cells positive for phosphorylated ribosomal protein-S6 with no change in quantity of myeloid cells (Fig. S14). In sum, our proteomic findings suggest that C3KO mice experience reduced mTORC1 activity through alterations in regulatory mechanisms which could explain why C3KO mice have reductions in inflammatory glia and reduced neuronal injury.

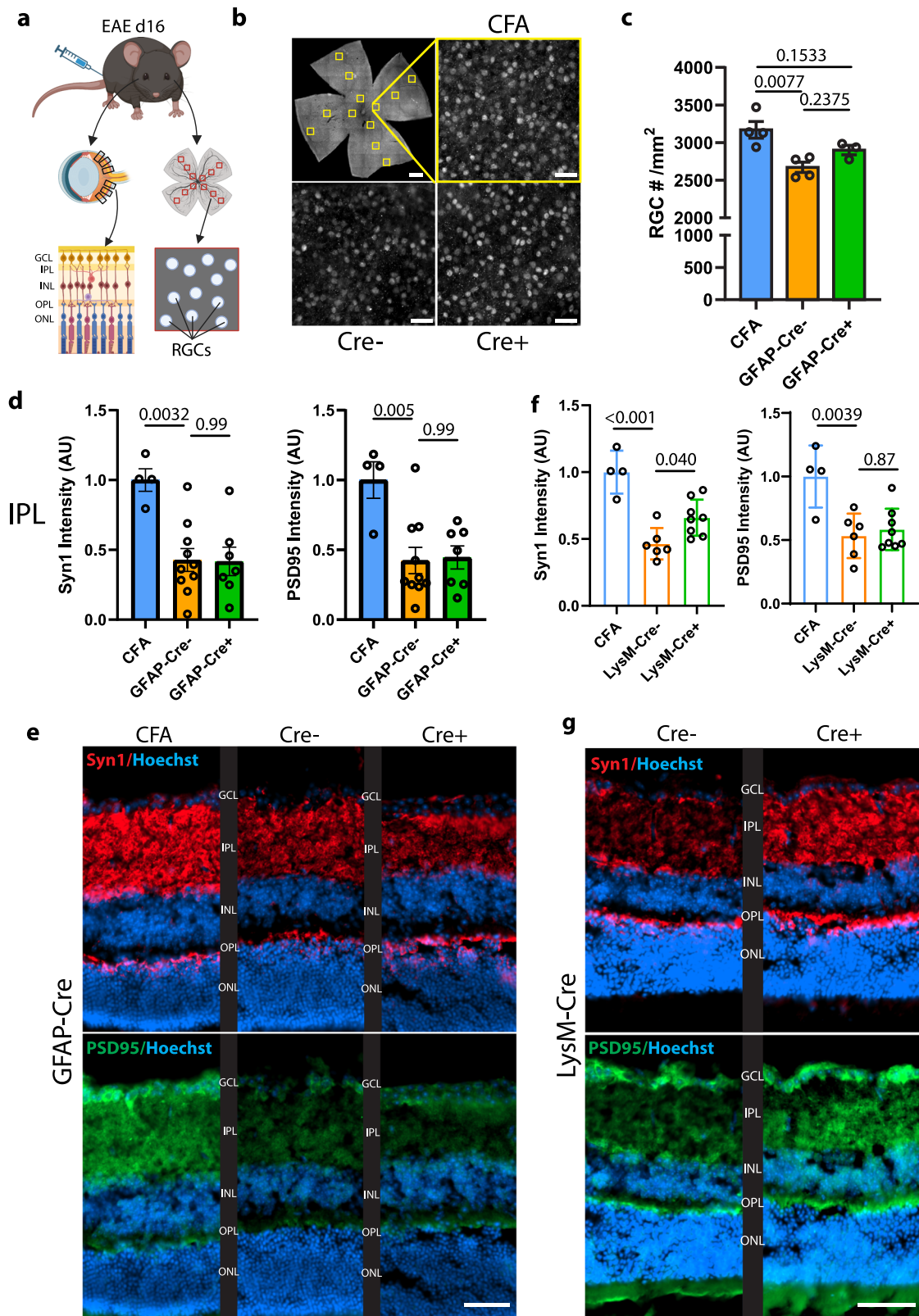
EAE mice exhibit significant retinal pathology at the peak of disease that is ameliorated by conditional knockout of myeloid but not astrocyte C3

While previous studies have demonstrated that both global C3 depletion as well as astroglial-specific C3 depletion has an effect on retinal ganglion cell (RGC) loss at the chronic stages of EAE (42 days post-immunization, approximately 4 weeks after disease score has peaked and by which point T-cell infiltrate in the optic nerve has fallen)¹³, our transcriptomic data suggests a dramatic effect of C3 on optic nerve glial phenotypes immediately following the peak of disease (16 days post-immunization, shortly after paralysis has peaked and at which point immune-infiltrate is high). We therefore sought to ascertain whether there was evidence of early neuronal insults potentially mediated by this C3-dependent pathologic phenotype. We first quantified RGC dropout at peak of EAE and tested whether this loss was dependent on astrocytic C3 using GFAP-Cre, C3-floxed mice to deplete C3 from GFAP-expressing astrocytes. Flat-mounted retinas revealed a mild yet significant loss of RGCs (identified with Brn3a

labeling) at day 16 post-immunization when comparing GFAP-Cre⁻ animals to CFA-only controls not immunized with MOG (Fig. 5b, c). GFAP-Cre⁺ animals surprisingly were not protected from RGC loss compared to Cre⁻ animals in contrast to what we have previously shown at the chronic timepoint (day 42)¹³. To confirm this finding of early RGC loss, we quantified with neuronal markers that are not downregulated in injury, namely γ -Synuclein (γ Syn) and Tuj1, and observed progressive RGC loss occurring at day 14 and continuing to day 21 (Fig. S15).

After observing this modest early neuron loss, we next characterized whether retinal synapses were being affected in the early stage of EAE by quantifying the synaptic proteins Synaptophysin1 (Syn1) and PSD95. Syn1 is a protein embedded in synaptic vesicles released from the presynaptic terminal of inner nuclear layer neurons and reflects the abundance of synaptic vesicles⁶¹, whereas PSD95 is a structural protein in the post-synaptic membrane of the RGCs and can therefore indicate physical synapse presence or loss⁶². Compared to the mild dropout of RGCs, both presynaptic (Syn1) and post-synaptic (PSD95) synaptic markers were significantly downregulated in the IPL of mice at peak EAE (Fig. 5d, e). Once again, however, deletion of C3 from astrocytes did not ameliorate this pathology (Fig. 5d, e). We further confirmed this finding of early synaptic loss using confocal imaging of retinas stained for PSD95 and Ribeye, the latter of which is a pre-synaptic component of synaptic ribbons (Fig. S16)⁶³. Similar to our observations using epifluorescent quantification of Syn1 and PSD95, confocal imaging showed loss of intact synapses (puncta colabeled with PSD95 and Ribeye) as well as an overall reduction in PSD95+ synaptic density when comparing MOG immunized WT mice with WT CFA controls at the peak of EAE. Indeed, the percent area positive staining of PSD95 as measured with confocal microscopy correlated well with PSD95 integrated density as measured with epifluorescent microscopy when measured on the same retina ($R^2 = 0.8508$, Fig. S17). We therefore used epifluorescent measurement of retinal synaptic markers for all further quantifications given its ability to measure larger sections of the retina.

Given the dramatic effect of C3KO on both microglia and infiltrating myeloid cells, we next used a LysM-Cre, C3-floxed system to deplete C3 from cells expressing the Lysozyme 2 gene, which includes both microglia and peripheral monocyte/macrophages but not astrocytes (Fig. S18). As we have previously demonstrated in both global C3KO and astrocyte-specific C3 depletion, the LysM-Cre;C3 floxed mice did not experience any differences in behavioral scores, indicating a similar inflammatory timeline and spinal cord damage to WT mice (Fig. S19). In these mice, Syn1 was significantly protected in the IPL whereas PSD95 levels were not changed (Fig. 5f, g). After observing this protection of pre-synaptic markers without a concomitant protection of post-synaptic markers in the LysM-Cre mice, we theorized that C3 derived by Lysozyme 2 producing cells was not directly causing physical synapse loss (as we would predict if the mechanism of action



was C3b-mediated synapse opsonization) but instead was influencing synaptic signaling in an alternative manner. It has been demonstrated that stressed or injured neurons can alter their synaptic signaling in an attempt to avoid excitotoxicity as part of an unfolded protein response⁶⁴, so we hypothesized that the reactive myeloid phenotype we observed in WT but that was decreased in C3KO may be involved in direct injury of RGCs potentially via insult to their axons in the optic

nerve and that any changes in synaptic signaling were a protective measure against excitatory/inhibitory balance alterations.

RGCs exhibit signs of myeloid C3-mediated neuronal stress and injury at peak EAE in conjunction with synaptic pathology

To assess whether these neurons were experiencing high levels of injury prior to their destruction and concurrently with their synapse

Fig. 5 | Retinas are affected at peak EAE (day 16) and exhibit signs of synaptic pathology that are ameliorated by depletion of myeloid but not astrocytic C3. **a** Diagram of experimental paradigm showing how eyes were either evaluated for synaptic pathology (left) via cross-sections or retinal ganglion cell (RGC) loss via flat mounts (right) on EAE d16 mice. **b** Representative image of flat-mounted retina with 12 regions selected for Brn3a⁺ RGC quantification. Scale bar in full retina image = 500 μm, in high magnification counting fields scale bar = 20 μm. **c** Quantification of Brn3a⁺ RGCs at peak EAE. *N* = 4 per experimental group. **d** Quantification of the integrated density of markers Syn1 (left) and PSD95 (right) in the inner plexiform layer of CFA vs GFAP-Cre animals at peak EAE. Signal intensity values are normalized to CFA control, with AU representing “arbitrary units”. *N* = 4 CFA, 10 GFAP-Cre⁺

and 7 GFAP-Cre⁺ mice. **e** Representative immunofluorescent staining of Syn1 (red) and PSD95 (green) in the inner and outer plexiform layers across GFAP-Cre experimental groups. Scale bar = 50 μm. **f** Same as in **e** but evaluating synaptic markers in the inner plexiform layer of LysM-Cre⁺ and LysM-Cre⁻ mice. Values are normalized to the CFA only animals utilized in Fig. 5d. *N* = 4 CFA, 6 LysM-Cre⁻ and 8 LysM-Cre⁺ mice. **g** Representative immunofluorescent staining of Syn1 and PSD95 in LysM-Cre⁻ vs LysM-Cre⁺ mice. Scale bar = 50 μm. All bar graphs presented as mean ± SEM, with one-way ANOVAs adjusted for multiple comparisons. Source data are provided as a source data file. Figure 5a created in BioRender. Smith, M. (2025) <https://BioRender.com/j21s335>.

loss, we quantified a marker of double stranded DNA breaks, γH2AX, in the RGCs of peak EAE animals. The percentage of RGCs with elevated levels of γH2AX was highly increased at peak EAE, which was not ameliorated in GFAP-Cre⁺ animals (Fig. 6a, b). However, the levels of γH2AX in the RGCs of LysM-Cre⁺ animals were reduced, again indicating that myeloid production of C3 mediates neuronal injury at this time point (Fig. 6c, d). Since the C3⁺ glia identified in the transcriptomic experiments above had upregulated genes related to oxidative stress and metabolically demanding pathways, we hypothesized that oxidative stress may contribute to RGC injury. We observed elevations of 8-OHdG, a marker of nucleic acid oxidation, in the RGCs of LysM-Cre⁻ mice at peak EAE, suggesting neuronal oxidative stress. This increased oxidative damage was ameliorated in LysM-Cre⁺ mice (Fig. 6e, f) and was concurrent with signs of axonal pathology in the optic nerve as evidenced by SMI32 staining, which again was reduced by myeloid C3 knockout (Fig. 6g, h). Altogether, this data suggests that deletion of myeloid but not astrocytic C3 reduces the high level of oxidative stress and dsDNA breaks in peak EAE RGCs concurrent with the previously demonstrated restoration of Synaptophysin 1, a marker of synaptic vesicles.

Discussion

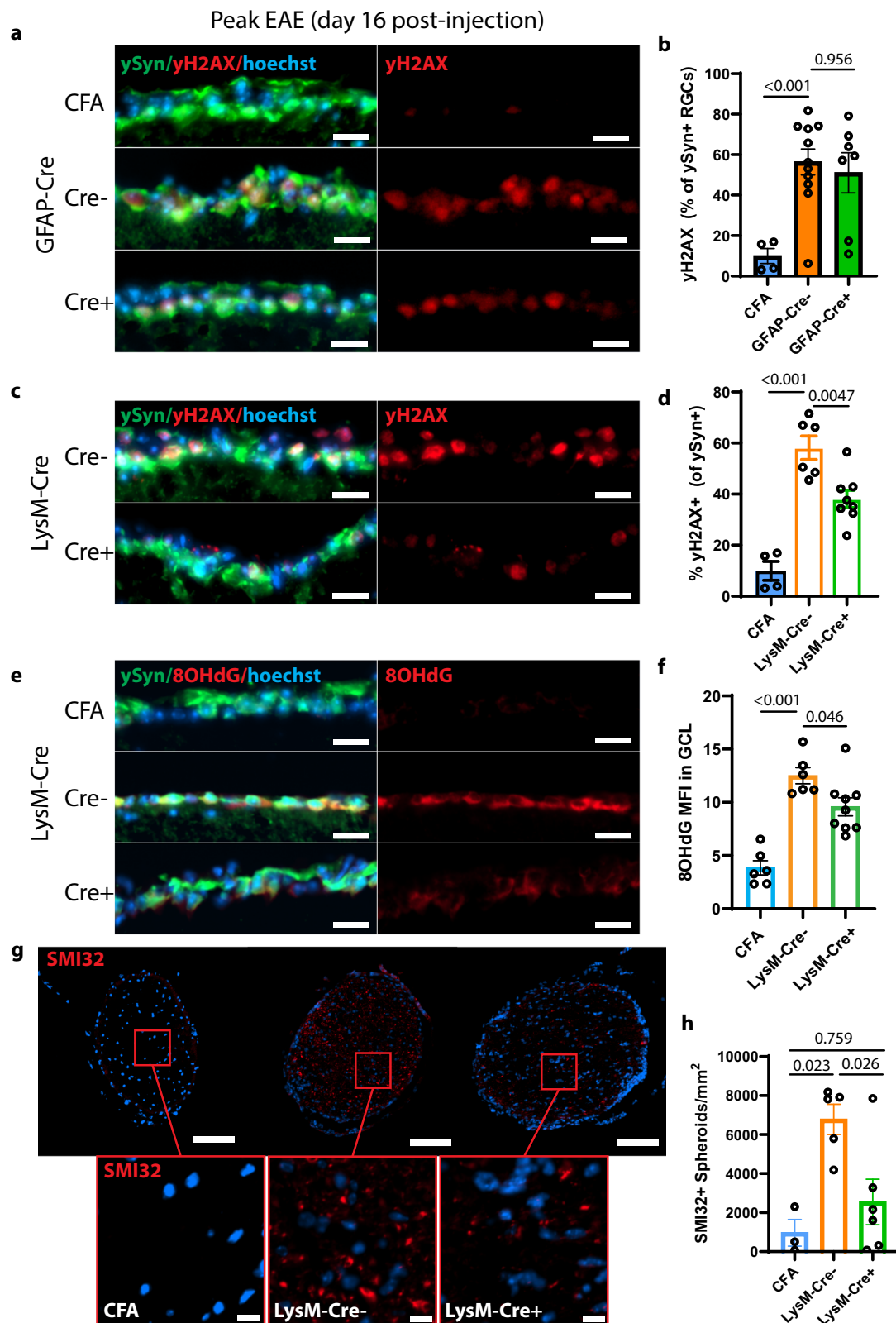
Herein, we utilized scRNAseq and C3 td-Tomato reporter mice to examine the transcriptomic profiles of subsets of macrophages, microglia, and astroglia from the CNS of WT and C3 KO mice at day 16 of EAE. We show that an early timepoint of EAE, before there is significant neurodegeneration, the phenotype of the glia is highly similar to the previously described microglial profile, called MIMS, which are in the edge of chronic active MS lesions¹⁰. Our ability to isolate these MIMS-like cells with C3 reporter-based sorting indicate that the most inflammatory subset of microglia in early EAE can be defined largely by their production of C3 itself, and we show that C3 deletion prevents the formation of this cell population. These C3⁺ microglia upregulate metabolically inefficient processes such as glycolysis while increasing their levels of translation and transcription of pro-inflammatory genes. C3 depletion resulted in a restoration of homeostatic phenotypes and a reduction in energetic pathways. Importantly, in this animal model, we did not observe any differences between C3⁺ and C3⁻ lymphocytes, nor did we identify any effect of C3 deletion on murine lymphocyte populations. We have shown previously that in our EAE studies there is no impact of C3KO on T cell infiltration nor EAE behavioral score—an indicator of global inflammation¹³. Therefore, it is likely that in models of CNS inflammation, the effects of C3 depletion are due at least in part to how C3's cleavage products can produce significant alterations in the transcriptomes of myeloid cells and local CNS glial cells. This makes targeting C3 a promising avenue for progressive MS, where local smoldering inflammation is largely unaffected by lymphocyte depletion or blocking cell trafficking.

Axonal transport disruption as a result of inflammatory demyelination has previously been suggested as a contributor to MS pathology^{65,66}, and our findings of increased SMI32 positive spheroids in the optic nerves suggests that RGCs may be vulnerable to axonal pathology earlier than anticipated. In keeping with the extensive

literature on the role for synaptic pruning in mediating neurodegeneration, our results could be explained by reduction in C3 mediated pruning of RGC dendrites. One would then need to speculate that this then modulates the optic nerve glia profiles in a manner to further suppress their activation. Indeed, we saw significant protection of synaptophysin in the inner plexiform layer in LysM-Cre mice vs WT, but no significant protection of PSD95, suggesting that myeloid-produced C3's contribution to excessive pruning may be less prominent. This discrepancy suggests that the role myeloid C3 plays in axonal damage and neuronal injury could result from an additional mechanism. We therefore think that consideration should be given to other mechanisms by which C3 deletion is preventing propagation of glial activation through paracrine or autocrine signaling.

The key molecular elements responsible for this propagation are still not fully determined. A recent study showed that stimulation of microglia with extracellular iC3b, the opsonizing form of C3, results in upregulation of some MIMS markers such as *C1qa* and *ApoE* as well as other pro-inflammatory markers such as *Lgals3* and *Ctsf*⁶⁷. It is therefore possible that depletion of C3 results in a reduction in MIMS via a reduction in extracellular iC3b signaling. In addition to C3b and iC3b, the other cleavage product C3a serves as a potent signaling molecule that can modulate global inflammation in a variety of contexts by binding to its receptor C3aR⁶⁸. This C3a-C3aR signaling has direct effects on a variety of cell types including mast cells, smooth muscle cells, and critically, CNS glial cells such as astrocytes and microglia^{69,70}. Several recent studies show C3aR depletion is beneficial in reversing HIF1a metabolic impairment and crossing C3ar1-knockout mice with the APP-K1 mice showed that C3aR ablation rescued the dysregulated lipid profiles⁷¹. In a recent study of a neuromyelitis optica lesion, in vivo spinal cord imaging revealed a striking physical interaction between microglia and astrocytes that required signaling from astrocytes by the C3a fragment of their upregulated complement C3 protein³⁹. Thus, we suggest C3a may be mediating some of the pathology seen in our experiments and warrants further investigation.

In addition to its role as an intercellular signaling agent, recently C3a has been shown to have functions intracellularly as part of the newly described complosome³¹. Interestingly, human T cells have been shown to utilize intracellular or autocrine C3 signaling to modulate mTOR activity resulting in their activation and polarization^{72–74}. The postulated mechanisms for this modality of complement signaling include intracellularly-localized complement receptors or potentially interactions between complement cleavage products with additional intracellular machinery^{73,74}. For instance, C3aR has been described as being stored intracellularly in granulocytes and macrophages⁷³. It therefore may be possible that the transcriptional changes in C3KO mice are instead due to a reduction of intracellular complement signaling. In our study, C3 deletion resulted in a reduction of pro-inflammatory genes in microglia, astrocytes, and monocytes/macrophages, perhaps due to reductions in genes downstream of mTOR signaling which modulates stress responses to amino acid deprivation⁷⁵. Targeting mTOR broadly in disease is a challenging proposition, since while it plays a role in generating inflammatory responses in certain cells like microglia and astrocytes^{76,77}, it promotes



autophagy-based survival in neurons⁷⁸. Therefore, recent discussion has arisen about identifying cell-selective mTOR inhibitors⁷⁹. We propose that targeting C3 might indirectly provide a way to selectively target mTOR in C3-producing CNS cells, which would allow for suppression of inflammatory signals without harming neuronal survival. Alongside reduction in pro-inflammatory genes, we observed marked downregulation of genes associated with metabolically demanding

processes in C3KO cells. Previous studies have suggested that promoting the integrated stress response in oligodendrocytes, which results in a global reduction in translation similar to what we observed in our C3KO cells, is protective in EAE^{80,81}.

As with any animal-based models of neuroinflammatory demyelination, there are some important limitations to consider when interpreting the results of our study. While myeloid cells (both

Fig. 6 | RGCs exhibit signs of myeloid C3-mediated neuronal injury both in the retina and in the optic nerve at peak EAE. **a** Representative immunofluorescent staining of γ H2AX (red) in the RGCs (γ Syn – green) in the ganglion cell layer of retinas from CFA as well as MOG-injected GFAP-Cre⁺ and GFAP-Cre⁻ animals at peak EAE. Scale bar represents 20 μ m. **b** Quantification of the percentage of RGCs that exhibit γ H2AX staining. $N = 4$ CFA, 10 GFAP-Cre⁻, and 7 GFAP-Cre⁺ mice. **c** As in (a) but for LysM-Cre⁺ and LysM-Cre⁻ animals. Scale bar represents 20 μ m. **d** Quantification of c. $N = 4$ CFA, 6 LysM-Cre⁻, and 8 LysM-Cre⁺ animals. CFA bar represents the same analysis as in 6b, as retinas were co-stained and analyzed simultaneously. **e** Representative immunofluorescent staining of 8-OHdG (red) in

γ Syn⁺ RGCs of CFA, LysM-Cre⁺, and LysM-Cre⁻ animals at peak EAE. Scale bar represents 20 μ m. **f** Quantification of (e). $N = 4$ CFA, 6 LysM-Cre⁻, and 9 LysM-Cre⁺ animals. **g** Representative immunofluorescent staining of SMI32⁺ axonal spheroids (red) in the optic nerves of CFA, LysM-Cre⁺, and LysM-Cre⁻ animals at peak EAE. Scale bar represents 100 μ m (or 10 μ m in high magnification inset). **h** Quantification of SMI32 density in optic nerves. $N = 3$ CFA, 5 LysM-Cre⁻, and 6 LysM-Cre⁺ animals. Each dot represents mean values from 3 different regions along the length of each optic nerve. For all comparisons, data presented as mean \pm SEM, with one-way ANOVA adjusted for multiple comparisons. Source data are provided as a source data file.

microglia and monocytes/macrophages) express very high levels of Lysozyme 2 and thus are efficiently targeted in the LysM-Cre transgenic mouse line, recombination with this Cre system has also been reported in neurons by multiple groups^{82,83} which means that in addition to myeloid cells, C3 depletion may also be occurring in neurons in the LysM-Cre;C3-floxed mouse line used here (Figs. 5, 6). How common neuronal production of C3 in the retina is unclear, a previous transcriptomic study of the mouse retina did not observe significant C3 production by retinal ganglion cells in either healthy or diseased mice³⁸. The fact that both microglia and peripheral myeloid cells express Lysozyme 2 also means that the effects we describe here, in both global KO and LysM-Cre targeted depletion, may still originate in the periphery. Despite the absence of effect on infiltrate quantity, T-cell Th1/Th17 polarization and disease score (Fig. S15)¹³, it is still possible the C3 depletion is affecting monocyte and macrophage phenotype first, and any effect observed in the local CNS cells is downstream of this effect⁸⁴. In addition, granulocytes also express Lysozyme 2 and have been shown to produce high levels of C3 in the setting of neuroaxonal injury⁸⁵. However, the fact that T-cells initiate the injury in EAE and circulating monocytes typically begin to differentiate upon infiltrating into the tissue suggests that at least some of the effects we observe is mediated by local C3 production in the CNS. Future studies with more cell-type specific depletion strategies will be needed to work out how each Lysozyme 2 producing cell population contributes to our observed C3 mediated pathology. Another caveat worth noting is that our experiments analyze an acute inflammatory response as opposed to the lengthy pathological processes that underlie chronic active MS lesions; however given the similarities between the mouse model transcriptomes and established transcriptomes from postmortem human samples, we believe there is value in studying the progression of chronic active lesions using an acute model. Throughout this report mice from both sexes were used in experiments. While we did not observe differences in the readouts by sex, it is possible that our sample sizes were too small to detect such differences. There is evidence for differences in circulating complement levels between males and females⁸⁶. However, how this translates to complement activity is not clear. When C3 activity specifically was examined in C57BL6 mice (the strain used here), no difference was observed between male and female mice⁸⁷. And in a recent EAE study, C3 levels were more highly induced in female compared to male optic nerve astrocytes⁸⁸. Our findings of C3-mediated early injury in such acute models could be of additional relevance for treating patients in the early stages of MS, including clinically isolated syndrome (CIS) and radiologically isolated syndrome (RIS). Subtle subclinical inflammation in CIS and RIS patients as detected by the presence of IL-8 in cerebrospinal fluid has been associated with a higher risk of disease progression to MS⁸⁹. Recognizing and treating early inflammation and neuronal stress in pre-symptomatic or early symptomatic patients may be key to preventing future disease progression. C3 inhibition in the retina has been discussed elsewhere⁹⁰, but the Phase III clinical trials OAKS (NCT03525613) and DERBY (NCT03525600) have demonstrated that intravitreal injections of the C3 inhibitor pegcetacoplan can reduce rates of geographic atrophy in the eye^{91,92}. It may be important to

consider CNS-penetrant C3 therapies early in the course of MS for reduction of neuronal pathology throughout the CNS.

In sum, with this work we identified a microglial subtype defined by C3 production in EAE that resembles MIMS observed in human disease and showed that C3 deletion has a marked effect on reducing the pathology-associated pro-inflammatory markers that define this and other reactive cell populations at both the transcript and protein level. We demonstrated the presence of neuronal injury and synaptic loss in the retinas of mice at the peak of EAE. Finally, we found that myeloid cells but not astrocytes producing C3 were involved in neuronal injury at the peak of EAE, suggesting that microglial complement is an early mediator of retinal pathology and that therapeutically targeting complement-producing microglia may be beneficial for neuroprotection, even in early MS.

Methods

Animals

All studies conducted as part of this work were reviewed and approved by the Animal Care and Use Committee at Johns Hopkins University under the protocol MO22M158. C57BL/6J mice (strain 000664) were purchased from The Jackson Laboratory. C3-tdTomato/floxed (C3^{tdT-*fl*}) reporter mice, which were recently described⁴⁰, were used to confirm C3 expression and conditionally deplete C3. Previously described mice deficient in C3 were utilized in the snRNA-seq experiment⁴⁰. GFAP-Cre;C3^{tdT-*fl*} mice were generated as described previously¹³. Additionally, LysM-Cre;C3^{tdT-*fl*} mice were generated by crossing the C3-tdTomato/floxed reporter mice with LysM-Cre mice purchased from The Jackson Laboratory (strain 004781). All animals were housed in the pathogen-free, temperature-controlled animal facility at the Johns Hopkins University School of Medicine with 12 h/12 h light/dark cycles and fed with standard food and water ad libitum. NIH guidelines for the use of experimental animals were exactly followed and all experimental protocols were approved by the Johns Hopkins Institutional Animal Care and Use Committee under protocol MO22M158.

EAE model

EAE was induced as described previously³⁶. All studies were carried out using 10–13 week-old mice. Briefly, mice were injected subcutaneously with 150 μ g of MOG₃₅₋₅₅ (Johns Hopkins Peptide Synthesis Core) in complete Freund's adjuvant (CFA) (ThermoScientific, Rockford, IL, USA) containing 600 μ g of mycobacterium tuberculosis (BD, Franklin Lakes, NJ) on the lateral abdomen. Control animals were injected with a CFA-only emulsion that lacked the MOG peptide addition. Concomitant with immunization and 2 days later, mice were also injected IP with 300 ng of pertussis toxin (List Biological Labs, Campbell, California, USA). Mice were sacrificed at the peak of disease, PID 16, using the drop method in which mice were exposed to high concentrations of isoflurane until they were unresponsive to noxious stimuli. Mice were then rapidly cardiac perfused with PBS then 4% paraformaldehyde followed by decapitation and tissue collection.

Clinical EAE behavioral scores were obtained daily, in a masked manner, using the established standard scoring from 1–5; 0 = no signs of disease; 1 = loss of tail tonicity; 2 = loss of tail tonicity and mild paralysis of hindlimbs; 3 = paralysis of hindlimbs; 4 = hindlimbs

paralysis and mild paralysis of forelimbs; and 5 = complete paralysis or death.

For immunohistochemical analyses of mouse RGC counts, $N = 3$ GFAP-Cre⁺ mice (average final EAE score 2 ± 1.08 ; sex = 100% male) and $N = 4$ GFAP-Cre⁻ (average final EAE score 2.875 ± 0.22 ; sex = 0% male) were compared to $N = 4$ CFA injected controls (EAE score = 0). For immunohistochemical analysis of synapse markers, $N = 7$ GFAP-Cre⁺ mice (average final EAE score 2 ± 0.76 ; sex = 42.85% male) were compared with $N = 10$ GFAP-Cre⁻ mice (average final EAE score 2.3 ± 0.6 ; sex = 10% male) with 4 CFA injected controls. For LysM-Cre analyses, $N = 8$ LysM-Cre⁺ mice (average final EAE score 1.32 ± 0.242 ; sex = 0% male) were compared to $N = 6$ LysM-Cre⁻ mice (average final EAE score 1.75 ± 0.56 ; sex = 50% male) with 4 CFA injected controls.

Mouse retina and optic nerve sample preparation

Mouse retina and optic nerves were collected as described previously³⁶. Briefly, after being sufficiently anesthetized by inhalation of evaporated isoflurane in a sealed container, mice underwent rapid cardiac perfusion with 30 mL phosphate buffered saline (PBS). After PBS perfusion, the eyes and attached optic nerves were removed from the eye socket by blunt enucleation using curved dressing forceps and immediately placed into 4% paraformaldehyde (PFA) for immersion fixation for four hours then transferred into 30% sucrose for cryoprotection. Mice were then perfused with 4% PFA and decapitated.

Optic nerves were separated from the eyes and evenly divided into three parts and then vertically placed into TissueTek mold filled with O.C.T. and snap frozen on dry ice. Frozen samples were stored at -80°C until cryosectioning. Optic nerves were sectioned at $10\ \mu\text{m}$ thickness and then mounted on slides for further immunofluorescence staining.

Whole flat mount retinas and vertical sectioned retinas were prepared as described using paired eyes from a single mouse as we previously showed RGC counts across retinas are the same within an EAE mouse³⁶. Flat mount retinas were processed for RGC labeling with anti-Brn3a (Pou4f1) antibody. After staining, the whole retinas were flat mounted onto slides and imaged for RGC counting. For vertical sectioned retinas, the eyes were placed into TissueTek mold filled with Optimal Cutting Temperature (O.C.T.) compound (VWR, Radnor, PA, USA), snap frozen by placing on dry ice and then stored at -80°C until cryosectioned. The eyes were sectioned at $16\ \mu\text{m}$ vertically and then mounted onto slides (ThermoScientific, Rockford, IL, USA) followed by staining with antibodies.

Immunofluorescence staining

All immunofluorescence staining protocols are previously published³⁶. Briefly, mice were deeply anesthetized by inhalation of a high concentration of isoflurane in a sealed container followed by rapid cardiac perfusion with PBS then 4% PFA before decapitation and tissue collection. Tissue sections were permeabilized with PBS containing 0.4% of Triton X-100 then blocked with PBS containing 5% normal goat serum and 0.1% Triton X-100 for 1 h at room temperature and incubated with primary antibody of interest overnight at 4°C . The primary antibodies that were used were Rabbit anti-Brn3a (Synaptic Systems, 411003; 1:1000), Rabbit anti-mouse PSD95 (abcam, ab18258; 1:1000), Chicken anti-mouse Synaptophysin1 (Synaptic Systems, 101006; 1:500), Rabbit anti-CD3 (Dako, A0452; 1:200), Rabbit anti-mouse IBA1 (Wako, 019-19741; 1:500), Chicken anti-IBA1 (Encor CPCA-IBA1; 1:1000), Mouse anti-TMEM119 (Synaptic Systems, 400 011; 1:500), Mouse anti- γH2AX (Thermo Scientific, MA1-2022; 1:400), Mouse anti-Tubulin βIII (Biolegend; 1:500) Rabbit anti- $\gamma\text{Synuclein}$ (γSyn) antibody (custom; via Covance as discussed elsewhere⁹³), Mouse anti-DAP12 (*Tyrbp*) (Santa Cruz, sc-166085; 1:400), Rat anti-CD68 (Thermo Scientific, 14-0681-82; 1:300), Mouse anti-SMI32 (BioLegend 801701; 1:500), Mouse anti-8OHdG (R&D Systems 4354-MC-050; 1:400), and Rabbit anti-Phospho-S6 Ribosomal Protein (Cell Signaling Technology

#4858; 1:100). The sections were then incubated for 1 h at room temperature with species-specific secondary antibodies directly conjugated to Alexa fluorophores (1:1000, Invitrogen) followed by nuclei staining with Hoechst. A coverslip was mounted onto sections using aqua poly/mount reagent (Polysciences, Warrington, PA, USA). Images were captured using a Zeiss Axio Observer Z1 epifluorescence microscope and Axiovision software with the appropriate excitation and emission filters. For confirmation of microglial expression of key markers in mouse brain, images were taken using a Zeiss 900 Confocal Microscope.

For all mouse retinal synaptic marker quantifications, the IPLs of six equidistant $145\ \mu\text{m}$ -wide ROIs per retina were analyzed using ImageJ software (Fig. S20). IPLs were outlined using the Hoechst nuclear stain to identify the nuclear layer boundaries. Intensity of staining was measured using Raw Integrated Density. To confirm correlation of Raw Integrated Density analysis with confocal percent area positive methods, we imaged retinas at peak EAE on a Zeiss 900 Confocal Microscope at 63x and performed consistent thresholding with ImageJ on the IPL region to determine the percentage of the IPL that stained positive for PSD95. For quantification of γH2AX , each RGC (denoted as γSyn^+ cells) along the length of an entire retina was assessed for the presence or absence of γH2AX signal. For 8OHdG signal intensity quantification, 6 equidistant regions were selected per retina as previously described and the MFI of 8OHdG was calculated in the ganglion cell layer. ImageJ software was used to quantify mean fluorescent intensity of the immunofluorescent signal by persons blinded to sample information. For optic nerve, three cross sectional regions were quantified as previously described³⁶.

To confirm the reduction in post-synaptic density in the IPL, Imaris10 software was used to analyze confocal images of retinas from mice at peak EAE (day 16) that were stained for the presynaptic marker Ribeye (clone 2D9 kindly gifted by the Frank Schmitz lab, located in ribbon synapses between interneurons and RGCs) and PSD95. In brief, retinas were sectioned and stained as previously described. Four regions sized $33.7\ \mu\text{m} \times 33.7\ \mu\text{m} \times 2.5\ \mu\text{m}$ were placed in the center of each retina and imaged at 63x with $0.1\ \mu\text{m}$ step size. Iterative analysis was performed by highlighting first Ribeye⁺ synapses with the circle drawing mode on multiple z-stack sections throughout each region, highlighting negative space, and then repeating that analysis for PSD95⁺ regions. The locations where there was a non-zero overlap between Ribeye⁺ and PSD95⁺ punctae were analyzed for density of intact synapses.

RGC counts

To count RGC number in whole retina, a mosaic image of the whole mount retina was captured using a Zeiss Axio Observer Z1 epifluorescence microscope with a motorized stage and a z-stack step size of $1\ \mu\text{m}$. After the images were acquired, each retinal quadrant was segmented into central, middle, and peripheral regions and 4 areas were counted per region, as shown in Fig. 5b and described previously³⁶. Our MATLAB-based semi-automated RGC counting algorithm was used to determine RGC number in each mouse³⁶. Briefly, selected segments were exported as tagged image file format (TIF) and fed into a custom MATLAB (Mathworks, Natick, MA, USA) size segmentation algorithm to perform automated counts. Cells in selected retinal segments undergo filtering, automatic or user-defined thresholding, and binarization followed by identification of cell boundaries. Labeled RGCs were counted at 20X magnification and a total of twelve regions were averaged to represent RGC density for each mouse retina. All analyses were performed masked to genotype and behavior score and data underwent quality control check.

Single cell isolation

Two new single-cell RNA transcriptomic experiments are described in this paper (in addition to the new single nucleus RNA sequencing

experiment experiment described below) – probe-based RNA profiling (Figs. 1, 2) and 3' Poly-A myeloid C3 reporter (Fig. S4).

Single cell isolation and FACS – probe-based RNA profiling (Figs. 1, 2, S1–S3). 6 C3 reporter animals (3 M, 3 F) were sacrificed at day 18 post-immunization (EAE scores: 2.5,2.2,5.1,5.2,1.5). Mice were euthanized by exposure to a high concentration of evaporated isoflurane in a sealed container then rapidly cardiac perfused with chilled Hanks Balanced Salt Solution (HBSS) without cations containing triptolide (10 μ M Sigma-Aldrich, cat T3652-IMG), anisomycin (27.1 μ g/mL, Sigma-Aldrich, cat A9789-5MG), and actinomycin D (5 μ g/mL, Sigma-Aldrich, cat A1410-2MG) to prevent papain induced transcriptional artifacts as previously described⁹⁴ followed by decapitation. Brains were dissected out from skulls and spinal cords were flushed from columns with hydrostatic pressure into the same HBSS used to perfuse. Tissue was then chopped into small pieces and transferred into digestion buffer (20 U/mL Papain (Worthington Biochemical, cat LS003120), 100 U/mL Deoxyribonuclease I (Worthington Biochemical, LS002006), 22.5 mM D(+) glucose, 26 mM NaHCO₃, 0.5 mM EDTA, 1mM L-cysteine, 10 μ M triptolide, 27.1 μ g/mL anisomycin, 5 μ g/mL actinomycin D in Earle's Balanced Salt Solution with pH adjusted to 7.41). Tissue was dissociated at 37°C under slow rotation for 30 min with manual trituration every 10 min. Following dissociation, tissue was passed over pre-wet 100 μ m filters which were washed with additional HBSS with cations. Dissociated tissue was then centrifuged at 300 g for 10 min, then resuspended in chilled Phosphate Buffered Saline (PBS). Myelin was removed using Myelin Removal Beads II (Miltenyi Biotec, cat 130-096-731). Dissociated cell pellets were resuspended in 2.34 mL MACS buffer (0.5% Bovine Serum Albumin, 2 mM EDTA in PBS) and 260 μ L of Myelin Removal Beads were added. Cells and beads were mixed and incubated for 15 min at 4°C then washed with 13 mL MACS buffer and centrifuged at 300 g for 10 min. Supernatant was removed and cell pellet was resuspended in 4 mL MACS Buffer. Each 4 mL sample was then passed over 4 separate pre-wetted LS columns (Miltenyi Biotec, cat 130-042-401), 1 mL per column. LS columns were then washed twice and then eluted with 1 mL MACS buffer. All flowthrough from the 4 columns per sample containing the myelin free cells was collected and pooled. Cells were then centrifuged at 300 g for 10 min and resuspended in chilled PBS then counted by flow cytometer. From the initial 6 mice, 3 pools were created by combining 2 mice per pool. Pool 1 was 2 F, Pool 2 was 2 M, and Pool 3 was 1 M and 1 F (individual cell counts per mouse in Supplemental Data 1). Following pooling, cells were incubated with an Fc blocking antibody (clone S17011E, Biolegend, cat 156604) at 1:200 and Live/Dead Violet at 1:1000 (Life Technologies cat L34963) in PBS for 20 min. Cells were washed with 0.1% BSA in PBS and then stained with surface antibodies in 0.1% BSA. Surface antibodies included Anti-ACSA2 APC at 1:50 dilution (clone REA969, Miltenyi Biotec, cat 130-116-245) Anti-CD45 APC-Fire750 (clone 30-F11, Biolegend, cat 103154) and Anti-CD11b BV510 at 1:500 dilution (clone MI170, Biolegend, cat 100353). After 30 min in surface stain, cells were washed with 0.1% BSA and resuspended in 0.1% BSA and sorted on a BD Fusion (4 laser – V/B/Y/R) at the SKCCC High Parameter Flow Core using a 100 μ m nozzle using gates as described in Supplemental Fig. 1a. The CD45⁻;ACSA2⁺;C3-tdT⁺ population was too small to be sorted on its own (given the number of washing steps that were required following the sort), so the sorting gate for the CD45⁻;ACSA2⁺;C3-tdT⁺ and C3-tdT⁻ population was drawn in such a way to capture all of the C3-tdT⁺ cells and only a small fraction of the C3-tdT⁻ cells. This was in an effort to enrich for the rarer C3-tdT⁺ population relative to the larger C3-tdT⁻ population.

Single cell isolation and FACS – 3' Poly-A Myeloid scRNAseq (Fig. S4). 4 C3 reporter animals (3F, 1M) were deeply anesthetized by exposure to a high concentration of evaporated isoflurane in a sealed container then rapidly cardiac perfused with chilled HBSS without

cations containing triptolide, anisomycin, and actinomycin D followed by decapitation and dissociated at day 18 post-immunization (EAE scores: 3,3,3,2,5) as in the probe-based RNA profiling, except only brains and not spinal cords were extracted and dissociated. In addition, instead of myelin removal beads, myelin was removed using Debris Removal Solution (Miltenyi Biotec, 130-109-398) by resuspending the cell pellet in 4.3 mL chilled PBS, then adding 1.25 mL Debris Removal Solution and mixing by pipetting 10 times. Cells were then overlaid with 4 mL chilled PBS and spun 3000 g for 15 min with medium acceleration and brake. The supernatant was aspirated all the way to the pellet and the tube was filled with 15 mL chilled PBS. Cells were then spun again at 1000 g for 10 min with full brake and acceleration. Supernatant was again aspirated and cells were resuspended in 500 μ L chilled PBS then all 4 mice were pooled into a single sample prior to proceeding to fluorescence-activated cell sorting (FACS). FACS was performed as in the probe-based RNA profiling except the CD11b antibody was conjugated to PerCP-Cy5.5 (Biolegend 101228), the live/dead stain was Live/Dead NIR (Life Technologies L34975), and cells were sorted into two populations – CD45⁺;CD11b⁺;C3-tdTomato⁺ and CD45⁺;CD11b⁺;C3-tdTomato⁻ (cell counts in Supplemental Data 1) on a BD FACS Aria III (3 laser – V/B/R) at the JHU Ross Flow Cytometry Core.

Single nuclei isolation

For the new single nucleus RNA sequencing data from the optic nerve experiment (Fig. 3), either wild type or C3 knockout mice were euthanized at day 16 post immunization by exposure to a high concentration of evaporated isoflurane in a sealed container until sufficiently anesthetized then were rapidly cardiac perfused with chilled HBSS. Eyeballs were enucleated and optic nerves detached and flash frozen in liquid nitrogen then stored at liquid nitrogen long term. Mice were then cardiac perfused with 4% PFA followed by decapitation. When sufficient samples had been collected, optic nerves were retrieved from liquid nitrogen and nuclei were isolated using 10X Chromium Nuclei Isolation Kit (10X Genomics, cat 1000493) according to manufacturer's recommendations but with some modifications. Briefly, optic nerves were mechanically dissociated in Lysis Reagent (10X genomics, cat 2000558) with Surfactant A (10X genomics, cat 2000559), Reducing Reagent B (10X genomics, cat 2000087) and RNase Inhibitor (10X Genomics, cat 2000565) using a glass Dounce homogenizer (Sigma-Aldrich, cat D8938-1SET), with 20 twists using large pestle then 15 twists using small pestle. Samples were transferred to a Nuclei Isolation Column (10X Genomics, cat 2000562) and centrifuged at 16,000 G for 20 s at 4 °C. Column was discarded and flow-through briefly vortexed and then transferred to pre-chilled 5 mL conical and centrifuged for 3 min at 500 g and 4 °C. Supernatant was aspirated and pellet was resuspended in 500 μ L Debris Removal Reagent (10X Genomics, cat 2000560) and centrifuged for 10 min at 700 g and 4 °C. The top portion of the supernatant was aspirated and the remaining supernatant and nuclei pellet were centrifuged again for 10 min at 150 g and 4 °C. Supernatant was completely aspirated and nuclei were resuspended in 2 mL Wash Buffer (1% BSA in PBS with RNase Inhibitor). Nuclei were then centrifuged one final time at 500 g, 4 °C, supernatant was removed, and nuclei were resuspended in 30 μ L nuclei resuspension buffer (1X Nuclei Buffer (10X genomics, cat 2000207), 1:1000 Reducing Agent B, 1:40 RNase Inhibitor) in nuclease-free water.

Single cell and nuclei partitioning and RNA-seq library preparation

Probe-based RNA profiling (Figs. 1, 2, S1, S2). For the Probe-based RNA samples (Figs. 1, 2), following FACS 9 samples (3 cell types per pool, 3 pools) were centrifuged then resuspended in 1 mL Fixation Buffer (4% Formaldehyde (ThermoFisher, cat BP531-25), 1X Conc. Fix and Perm Buffer (10X Genomics, cat PN-2000517) in nuclease free

water) and left overnight at 4 °C (Sorted counts available in Supplemental Data 1). The next morning the samples were centrifuged, supernatant removed, and cell pellet resuspended in 1 mL quenching buffer (10X Genomics, cat PN-2000516). Then 100 µL of Enhancer (10X Genomics, cat 2000482) and 275 µL 50% glycerol were added and samples were stored at -80 °C until processing. Samples were later thawed at the Johns Hopkins Single Cell and Transcriptomics Core and processed according to manufacturer's recommendation for Chromium Fixed RNA Profiling using Multiplexed samples. Steps consisted of probe hybridization (where each probe is barcoded to a particular sample) followed by a post-hybridization cell count. The 9 samples were then pooled equally (22,750 cells per sample) and washed. GEM generation and barcoding were performed using a Chromium Next Gem Chip Q, which was run in a Chromium X controller, followed by library construction. Which probe barcode corresponds to which sample is included in Supplemental Data 1.

3' chemistry (Fig. S3). For the myeloid C3 reporter (Fig. S3), following FACS cells were centrifuged then resuspended in 0.1% BSA and counted on hemocytometer. Cells were then loaded onto a Chromium Next Gem Chip G and GEMs were generated using 10X Genomics Single Index 3' v3.1 chemistry according to manufacturer's recommendation. The GEM generation and library preparation was done at the Johns Hopkins Single Cell and Transcriptomics Core.

Multiome. The optic nerve nuclei dataset was generated using the 10X Genomics MultiOme ATAC + Gene Expression kit (cat 1000285). Following nuclei isolation (as detailed in "Single Nuclei Isolation" above), nuclei were counted on a Countess 3 FL automated cell counter (Life Technologies) in 1 µg/mL acridine orange using a GFP light cube. We counted 14,910 (WT-1), 103,500, (WT-2) 57,000 (KO-1), and 30,000 (KO-2) nuclei for the 4 samples. For samples WT-1, KO-1, and KO-2 we transferred 5 µL of nuclei (-1543, 5901, and 3106 nuclei respectively) into 10 µL transposition mix (7 µL ATAC Buffer B (10X Genomics, cat 2000193)), 3 µL ATAC Enzyme B (10X Genomics, cat 2000272). For sample WT-2 we only transferred 2.84 µL (-6086 nuclei) and 2.16 µL of the nuclei resuspension buffer to avoid having too much variability in nuclei number between the samples. The 15 µL (5 µL nuclei, 10 µL transposition mix) were pipette mixed 6 times (pipette set to 10 µL), and then incubated at 37 °C for 60 min in a C1000 touch thermal cycler (Bio-Rad) with reaction volume set to 15 µL and lid set to 50 °C. Nuclei were then loaded onto Chromium Next Gem Chip J and partitioned into GEMs on a Chromium Controller. Both gene expression and ATAC libraries were then prepared according to manufacturer's recommendation. While the ATAC data were of high quality, there were insufficient nuclei to find convincing differences between the WT and KO datasets given the sparsity of the ATAC data. These analyses were not included in this paper, but the raw sequencing data and fragment quantification is available in the GEO repository.

Library sequencing. All transcriptomic libraries were sequenced on an Illumina NovaSeq 6000 at the Johns Hopkins Single Cell and Transcriptomics Core according to Illumina and 10X Genomics recommendations. The Probe-based RNA Profiling and optic nerve nuclei Multiome Gene Expression libraries were sequenced on S4 200 flow cells as follows: Read 1: 28 base pairs (bp), i7 Index: 10 bp, i5 Index: 10 bp, Read 2: 91 bp. The myeloid C3 reporter libraries were sequenced on an S4 200 flow cell as follows: Read 1: 28 bp, i7 Index: 8 bp, Read 2: 91 bp. The CD45⁻ C3 Reporter 3' library was sequenced on an S2 100 flow cell as follows: Read 1: 28 bp, i7 Index: 10 bp, i5 Index: 10 bp, Read 2: 90 bp. The optic nerve nuclei Multiome ATAC libraries were also sequenced on a NovaSeq 6000 using an S4 200 flow cell as follows: Read 1 N (R1): 50 bp, i7 Index (I1): 8 bp, i5 Index (R2): 24 bp, Read 2 N (R3): 50 bp. Fastq files from all sequencing reads

were generated when data was uploaded to the Basespace Sequencing Hub (Illumina).

Generation of expression matrices from sequencing data. Fastq files from Illumina Sequencing Hub were processed using Cell Ranger (10X Genomics) to generate gene expression matrices. The optic nerve nuclei from the Multiome library preparation were processed with cellranger-arc count (v2.0.2) against mm10-2020-A reference provided by 10X Genomics with "Include introns" option set to True. The Probe-based RNA Profiling libraries were processed with cellranger multi (v7.1.0) using 10X provided mm10-2020-A reference and Chromium Mouse Transcriptome Probe Set v1.0.1. The 3' Myeloid C3 reporter libraries were processed with cellranger count (v7.0.1) ("Include introns" set to True) against a custom reference generated with cellranger mkref that added the sequence for tdTomato and EGFP (called TDT and GFP in reference) to the Ensembl GRCm39.104 transcriptome⁹⁵.

Transcriptomic data processing

Expression matrices generated by Cell Ranger were primarily processed in R (v.4.2.3) with the package Seurat (v4.3.0.1)⁹⁶ with additional functionality being provided by R packages SingleCellExperiment (v1.20.1)^{97,98}, scuttle (v1.8.4)⁹⁷, scran (v1.26.2)⁹⁹, scDblFinder (v1.12.0)¹⁰⁰, scCustomize (v1.1.3)¹⁰¹, and edgeR (v3.40.2)¹⁰². For all datasets, the cell count, average UMI count, median feature count, and mean mitochondrial ratio both before and after quality control are listed in Supplemental Data 1.

Probe-based RNA Dataset comparing C3⁺ Myeloid, C3⁻ Myeloid, and CD45⁻;ACSA2⁺ Cells. Filtered feature counts were imported into R with Seurat's *Read10X_h5* function then converted to Seurat Objects with *CreateSeuratObject* using default options. The ratio of detected transcripts mapping to mitochondrial genes was calculated with Seurat's *PercentageFeatureSet* function. For each individual sample ($n=9$), poor quality cells were identified with the *perCellQCFilter* function from the scuttle package which identifies outliers for UMI count, feature count, and mitochondrial ratio as being more than 3 median absolute deviations from the median. Outliers were then removed from each dataset. Doublets were predicted with *scDblFinder* using default settings on each individual sample and the predicted doublet score and class were then added to each cell's metadata. The predicted doublets were retained to help identify likely doublets in downstream analyses that did not rise to the threshold of being called a doublet. The 9 datasets were then merged into a single dataset and UMI count data was normalized with a regularized negative binomial regression with Seurat's *SCTransform* function using default parameters. Using the normalized dataset, we then used Seurat to run principle component analysis (*RunPCA*), perform uniform manifold approximation and project (UMAP) dimensionality reduction (*RunUMAP*, using first 30 principle components), create a nearest neighbor graph (*FindNeighbors*, using first 30 principle components), and identify clusters based on the nearest neighbor graph using the original Louvain algorithm (*FindClusters*). Cell types were then identified based on marker gene expression and subsetted to cell types of interest (astrocytes, microglia, monocytes/macrophages) (Fig. S2b, f). Subclustering was then performed on these cell subsets by repeating the above analyses on only the cells of interest, except using the *glmGamPoi*¹⁰³ method instead of the default poisson in the UMI normalization and resolution for *FindClusters* was set to 0.8.

Optic nerve nuclei comparing C3 WT vs C3 KO. Filtered feature counts were processed identically as for the probe-based RNA dataset above, but with 4 samples ($n=2$ WT, $n=2$ KO). The negative binomial transformation used the *glmGamPoi* method for the UMI count

normalization of both the full dataset as well as in the subclustering analyses. The UMAP and nearest neighbor graph for the full dataset were constructed with the first 29 principal components. Cell type subsets were subclustered as in the probe-based RNA dataset (Fig. S7b).

3' Myeloid C3 reporter and 3' CD45- C3 reporter datasets. Both of these datasets were analyzed similarly to those above. Both contained 2 libraries, a C3-tdT⁺ sorted population and a C3-tdT⁻ sorted population. Poor quality cells were identified as those greater than 3 median absolute deviations from the median for UMI count, Feature Count, or mitoRatio except for the CD45⁻ C3 reporter dataset, for which we used an absolute value of 15% as the upper threshold for mitochondrial ratio. After quality control was performed for each individual library as described above, the positive and negative populations were merged into a single Seurat object and analysis proceeded as described above. For both datasets, 40 principal components were used for the nearest neighbor graph and Louvain clustering. Cell type subclustering was performed as described above.

Integration of transcriptomic datasets. For comparing C3 WT and C3 KO optic nerve nuclei with a dataset that included CFA controls, raw sequencing data was retrieved for the 3 EAE and 3 control 5' scRNA-seq libraries previously published by Fournier et al.⁵² under GEO accession GSE199460. Reads were aligned with Cell Ranger (v7.1.0) against the mm10-2020-A reference provided by 10X Genomics with "Include introns" set to True. The filtered feature counts were then imported into R using Seurat and QC was done similarly to the previously published analysis, with cells being removed that had a feature count less than 750 or greater than 5500 or a mitochondrial ratio greater than 10. Doublets were predicted on a per sample basis with scDblFinder but retained. Data were normalized and the microglia populations were subsetted. We then integrated three datasets using canonical correlation analysis (CCA) with Seurat's *IntegrateData* pipeline¹⁰⁴ – microglia from the merged C3 WT vs KO optic nerve nuclei dataset described above, the merged microglia from the 1st batch of samples in the Fournier dataset ($n=1$ EAE, 2 control) and the merged microglia from the 2nd batch of samples in the Fournier dataset ($n=2$ EAE, 1 control) after each dataset had independently been normalized for UMI count with *SCTransform*. Following integration, we ran PCA, created a nearest neighbor graph (with 1st 30 PCs), ran Louvain clustering, and performed UMAP analysis (with 1st 30 PCs) with Seurat. For comparing the optic nerve microglia (Fig. 3) with those from the brain (generated with 3' PolyA scRNAseq methodology, Fig. S4), the two subsetted microglia datasets were merged into a single Seurat object then integrated with canonical correlation analysis using the log normalized expression values¹⁰⁴. We then performed UMAP dimensionality reduction using the first 20 dimensions of the CCA integration followed by unsupervised clustering as described above (again with the first 20 dimensions) using a resolution of 0.4.

Pseudobulk differential expression testing. Differential expression testing was performed using the methodology of the *pseudoBulkDGE* function in the *scrans* package but was done step by step as previously described⁹⁸ rather than via the function call itself. Briefly, pseudobulk expression for each sample:cell type pairing was generated with Seurat's *AggregateExpression* function on the raw count data. These count matrices were then converted to DGEList objects with *edgeR* and lowly expressed genes were removed with the function *filterByExpr*. Per sample normalization factors were calculated (*calcNormFactors*) followed by estimated negative binomial dispersions (*estimateDisp*). We then fit a quasi-likelihood negative binomial model (*glmQLFit*, robust argument set to TRUE) and tested for differential expression between genotypes (or sort for the probe-based

RNA profiling experiment). Genes with a false discovery rate (FDR) adjusted p -value less than 0.05 were considered to be differentially expressed.

Marker gene identification. Marker genes for individual clusters throughout the transcriptomic datasets were identified using Seurat's *FindAllMarkers* function with default parameters. Marker genes for microglia subclusters included in Supplemental Data 3 were filtered on those that had adjusted p -values <0.05. For integrated datasets, Seurat's *FindConservedMarkers* function was used filtering on genes that were positive with a minimum percentage set to 0.25 and a log2Fold-change threshold set to 1.5.

GSEA analysis of differentially expressed genes. The gene-set enrichment analysis (GSEA) was performed using GSEA software version 4.3.2 using pre-ranked gene lists generated by the *edgeR* pseudobulk differential expression testing^{105,106}. When comparing microglial subclusters in Fig. 2, *FindAllMarkers* was used to generate a list of DEGs in each cluster which were subsequently sorted based on log 2-fold change, resulting in a ranked gene list. Normalized enrichment score and FDR were used to determine pathway enrichment significance. GSEA plots were visualized with the R package "ggplot2".

Pathway analysis with IPA. To determine which pathways were significantly enriched in key cell types, genes with FDR <0.05 (as determined with the *edgeR* pseudobulk differential testing) were analyzed using Ingenuity Pathway Analysis software (Qiagen, version 107193442). The top enriched pathways (smallest p -value) were plotted using the R package "ggplot2".

Differential abundance testing. Differential abundance testing was done with the *edgeR* package which uses a negative binomial generalized linear model^{98,102}. Abundances (% of each sample within each cluster) were used from each biological ($n=4$, 2 per genotype). The design formula tested for effect of genotype, ie \sim genotype. We estimated negative binomial dispersion with *estimateDisp* with trend set to none, then quasiliikelihood dispersion using *glmQLFit* with abundance.trend set to false, then tested for differences in abundance between genotypes with *glmQLFTest* and report p -values for each cluster adjusted for false discovery in Fig. S9.

Proteomic and phosphoproteomic analysis of the optic nerves of C3KO and WT EAE mice

For the proteomic and phosphoproteomic experiments, $N=7$ WT and $N=7$ C3KO mice that were given EAE until PID 16 were score matched and euthanized using a high concentration of evaporated isoflurane in a sealed container to achieve sufficient anesthetization followed by rapid cardiac perfusion with PBS after which their optic nerves were harvested and flash frozen. Mice were then perfused with 4% PFA and decapitated. In addition, $N=2$ WT and $N=2$ C3KO naïve mice were used as controls with the same protocol. Proteomic analysis, except for the phosphopeptide enrichment, was conducted as described previously with minor modifications. Optic nerves were lysed by sonicating in 8 M urea and 50 mM triethylammonium bicarbonate (TEAB). The samples were reduced and alkylated in 10 mM tris (2-Carboxyethyl) phosphine hydrochloride (TCEP) with 40 mM chloroacetamide (CAA) at room temperature (RT) for 1 h, followed by digesting them with LysC (lysyl endopeptidase mass spectrometry grade, Fujifilm Wako Pure Chemical Industries Co., Ltd., Osaka, Japan) at one-to-hundred ratio for 3 h at 37°C. After diluting urea concentration from 8 M to 2 M by adding 3 volumes of 50 mM TEAB, proteins were further digested with sequencing-grade trypsin (Promega, Fitchburg, WI, USA) at a one-to-fifty ratio at 37°C overnight. Peptides were desalted using C18 StageTips (3M EmporeTM; 3 M, St. Paul, MN, USA) and were labeled using TMTpro 18-plex reagents following the manufacturer's

instructions (Thermo Fisher Scientific, Waltham, MA, USA). These TMT-labeled peptides were pooled, with 25% allocated for total proteome analysis and the remaining 75% allocated for phosphopeptide enrichment.

The phosphopeptide enrichment was conducted using sequential enrichment using a metal oxide affinity chromatography (SMOAC) kit according to the manufacturer's instructions (Thermo Fisher Scientific, Waltham, MA, USA). Samples for total proteome analysis were pre-fractionated using basic pH reversed-phase liquid chromatography into 96 fractions and concatenated into 24 fractions; similarly, the enriched phosphopeptides were pre-fractionated into 96 fractions and concatenated into 12 fractions. The samples were analyzed on an Orbitrap Fusion Lumos Tribrid mass spectrometer interfaced with an Ultimate 3000 RS Autosampler nanoflow liquid chromatography system (Thermo Scientific). The acquired mass spectra files were fed into Proteome Discoverer (version 2.4.1.15, Thermo Scientific) to identify and quantify proteins by searching against the mouse UniProt database (released in December 2019) containing common contaminant proteins using SEQUEST HT algorithms.

Statistical analysis

Statistical analysis was conducted using GraphPad Prism software version 10.0.0 (GraphPad, San Diego, CA, USA). Unpaired two-tailed Student's *t*-test was used to analyze data with two comparative conditions. Ordinary one-way ANOVA was used to analyze datasets with multiple conditions. Results were considered significant if the *p*-value was <0.05. Error bars indicate SEM in all figures.

Reporting summary

Further information on research design is available in the Nature Portfolio Reporting Summary linked to this article.

Data availability

All raw sequencing data, as well as Cell Ranger generated filtered count matrices, newly generated in this manuscript are available in the Gene Expression Omnibus under the SuperSeries accession [GSE260984](https://www.ncbi.nlm.nih.gov/geo/query/acc.cgi?acc=GSE260984). The probe-based single cell data is available in the accession [GSE260982](https://www.ncbi.nlm.nih.gov/geo/query/acc.cgi?acc=GSE260982), the 3' myeloid data is available in the accession [GSE260983](https://www.ncbi.nlm.nih.gov/geo/query/acc.cgi?acc=GSE260983), and the optic nerve nuclei data (both gene expression and ATAC data) are available under the accession [GSE260978](https://www.ncbi.nlm.nih.gov/geo/query/acc.cgi?acc=GSE260978). The previously published 3' CD45- C3 reporter scRNA-seq dataset is available in the Gene Expression Omnibus under accession [GSE254863](https://www.ncbi.nlm.nih.gov/geo/query/acc.cgi?acc=GSE254863). The mass spectrometry data and search results from this study have been deposited to the ProteomeXchange via PRIDE partner repository with the dataset identifier 'PXD054869', project name 'Myeloid lineage C3 induces reactive gliosis and neuronal stress during CNS inflammation.' [<https://www.ebi.ac.uk/pride/archive/projects/PXD054869>]. Source data for immunofluorescent quantifications and EAE behavioral scores are provided in Source Data file. Source data are provided with this paper.

References

- Qian, K. et al. Revisiting the critical roles of reactive astrocytes in neurodegeneration. *Mol. Psychiatry* **28**, 2697–2706 (2023).
- Hickman, S., Izzy, S., Sen, P., Morsett, L. & El Khoury, J. Microglia in neurodegeneration. *Nat. Neurosci.* **21**, 1359–1369 (2018).
- Colonna, M. & Butovsky, O. Microglia function in the central nervous system during health and neurodegeneration. *Annu Rev. Immunol.* **35**, 441–468 (2017).
- Liddelow, S. A. et al. Neurotoxic reactive astrocytes are induced by activated microglia. *Nature* **541**, 481–487 (2017).
- Oechtering, J. et al. Complement activation is associated with disease severity in multiple sclerosis. *Neurol. Neuroimmunol. Neuroinflamm.* **11**, e200212 (2024).
- Bourel, J. et al. Complement C3 mediates early hippocampal neurodegeneration and memory impairment in experimental multiple sclerosis. *Neurobiol. Dis.* **160**, 105533 (2021).
- Werneburg, S. et al. Targeted complement inhibition at synapses prevents microglial synaptic engulfment and synapse loss in demyelinating disease. *Immunity* **52**, 167–182 e167 (2020).
- Healy, L. M., Stratton, J. A., Kuhlmann, T. & Antel, J. The role of glial cells in multiple sclerosis disease progression. *Nat. Rev. Neurol.* **18**, 237–248 (2022).
- Gleichman, A. J. & Carmichael, S. T. Glia in neurodegeneration: drivers of disease or along for the ride? *Neurobiol. Dis.* **142**, 104957 (2020).
- Absinta, M. et al. A lymphocyte-microglia-astrocyte axis in chronic active multiple sclerosis. *Nature* **597**, 709–714 (2021).
- Schirmer, L. et al. Neuronal vulnerability and multilineage diversity in multiple sclerosis. *Nature* **573**, 75–82 (2019).
- Britze, J., Pihl-Jensen, G. & Frederiksen, J. L. Retinal ganglion cell analysis in multiple sclerosis and optic neuritis: a systematic review and meta-analysis. *J. Neurol.* **264**, 1837–1853 (2017).
- Gharagozloo, M. et al. Complement component 3 from astrocytes mediates retinal ganglion cell loss during neuroinflammation. *Acta Neuropathol.* **142**, 899–915 (2021).
- Stephan, A. H., Barres, B. A. & Stevens, B. The complement system: an unexpected role in synaptic pruning during development and disease. *Annu Rev. Neurosci.* **35**, 369–389 (2012).
- Stevens, B. et al. The classical complement cascade mediates CNS synapse elimination. *Cell* **131**, 1164–1178 (2007).
- Soteros, B. M. & Sia, G. M. Complement and microglia dependent synapse elimination in brain development. *WIREs Mech. Dis.* **14**, e1545 (2022).
- Guttikonda, S. R. et al. Fully defined human pluripotent stem cell-derived microglia and tri-culture system model C3 production in Alzheimer's disease. *Nat. Neurosci.* **24**, 343–354 (2021).
- Escartin, C. et al. Reactive astrocyte nomenclature, definitions, and future directions. *Nat. Neurosci.* **24**, 312–325 (2021).
- Linnerbauer, M., Wheeler, M. A. & Quintana, F. J. Astrocyte crosstalk in CNS Inflammation. *Neuron* **108**, 608–622 (2020).
- Hong, S. et al. Complement and microglia mediate early synapse loss in Alzheimer mouse models. *Science* **352**, 712–716 (2016).
- Michailidou, I. et al. Complement C1q-C3-associated synaptic changes in multiple sclerosis hippocampus. *Ann. Neurol.* **77**, 1007–1026 (2015).
- Dejanovic, B. et al. Complement C1q-dependent excitatory and inhibitory synapse elimination by astrocytes and microglia in Alzheimer's disease mouse models. *Nat. Aging* **2**, 837–850 (2022).
- Tzioras, M. et al. Human astrocytes and microglia show augmented ingestion of synapses in Alzheimer's disease via MFG-E8. *Cell Rep. Med.* **4**, 101175 (2023).
- Wilton, D. K. et al. Microglia and complement mediate early corticostriatal synapse loss and cognitive dysfunction in Huntington's disease. *Nat. Med.* **29**, 2866–2884 (2023).
- Vasek, M. J. et al. A complement-microglial axis drives synapse loss during virus-induced memory impairment. *Nature* **534**, 538–543 (2016).
- Henstridge, C. M., Tzioras, M. & Paolicelli, R. C. Glial contribution to excitatory and inhibitory synapse loss in neurodegeneration. *Front Cell Neurosci.* **13**, 63 (2019).
- Popoli, M., Yan, Z., McEwen, B. S. & Sanacora, G. The stressed synapse: the impact of stress and glucocorticoids on glutamate transmission. *Nat. Rev. Neurosci.* **13**, 22–37 (2011).
- von Palffy, S. et al. The complement receptor C3AR constitutes a novel therapeutic target in NPM1-mutated AML. *Blood Adv.* **7**, 1204–1218 (2023).

29. Boos, L., Campbell, I. L., Ames, R., Wetsel, R. A. & Barnum, S. R. Deletion of the complement anaphylatoxin C3a receptor attenuates, whereas ectopic expression of C3a in the brain exacerbates, experimental autoimmune encephalomyelitis. *J. Immunol.* **173**, 4708–4714 (2004).
30. Boos, L., Szalai, A. J. & Barnum, S. R. C3a expressed in the central nervous system protects against LPS-induced shock. *Neurosci. Lett.* **387**, 68–71 (2005).
31. West, E. E. & Kemper, C. Complosome - the intracellular complement system. *Nat. Rev. Nephrol.* **19**, 426–439 (2023).
32. Friscic, J. et al. The complement system drives local inflammatory tissue priming by metabolic reprogramming of synovial fibroblasts. *Immunity* **54**, 1002–1021 e1010 (2021).
33. Weerth, S. H., Rus, H., Shin, M. L. & Raine, C. S. Complement C5 in experimental autoimmune encephalomyelitis (EAE) facilitates remyelination and prevents gliosis. *Am. J. Pathol.* **163**, 1069–1080 (2003).
34. Rus, H., Cudrici, C. & Niculescu, F. C5b-9 complement complex in autoimmune demyelination and multiple sclerosis: dual role in neuroinflammation and neuroprotection. *Ann. Med.* **37**, 97–104 (2005).
35. Quinn, T. A., Dutt, M. & Shindler, K. S. Optic neuritis and retinal ganglion cell loss in a chronic murine model of multiple sclerosis. *Front. Neurol.* **2**, 50 (2011).
36. Jin, J. et al. Glial pathology and retinal neurotoxicity in the anterior visual pathway in experimental autoimmune encephalomyelitis. *Acta Neuropathol. Commun.* **7**, 125 (2019).
37. Rutar, M., Valter, K., Natoli, R. & Provis, J. M. Synthesis and propagation of complement C3 by microglia/monocytes in the aging retina. *PLoS ONE* **9**, e93343 (2014).
38. Pauly, D. et al. Cell-type-specific complement expression in the healthy and diseased retina. *Cell Rep.* **29**, 2835–2848 e2834 (2019).
39. Chen, T. et al. Astrocyte-microglia interaction drives evolving neuromyelitis optica lesion. *J. Clin. Invest.* **130**, 4025–4038 (2020).
40. Kolev, M. et al. Diapedesis-induced integrin signaling via LFA-1 facilitates tissue immunity by inducing intrinsic complement C3 expression in immune cells. *Immunity* **52**, 513–527 e518 (2020).
41. Vallejo, A. F. et al. snPATHO-seq: unlocking the FFPE archives for single nucleus RNA profiling. *bioRxiv*. <https://doi.org/10.1101/2022.08.23.505054> (2022)
42. Jordao, M. J. C. et al. Single-cell profiling identifies myeloid cell subsets with distinct fates during neuroinflammation. *Science* **363**, eaat7554 (2019)
43. Lund, H. et al. Competitive repopulation of an empty microglial niche yields functionally distinct subsets of microglia-like cells. *Nat. Commun.* **9**, 4845 (2018).
44. Groh, A. M. R. et al. Ependymal cells undergo astrocyte-like reactivity in response to neuroinflammation. *J. Neurochem.* **168**, 3449–3466 (2024)
45. Lee, J. Y. et al. Serum amyloid A proteins induce pathogenic Th17 cells and promote inflammatory disease. *Cell* **183**, 2036–2039 (2020).
46. De Schepper, S. et al. Perivascular cells induce microglial phagocytic states and synaptic engulfment via SPP1 in mouse models of Alzheimer’s disease. *Nat. Neurosci.* **26**, 406–415 (2023).
47. Wang, S. et al. S100A8/A9 in Inflammation. *Front. Immunol.* **9**, 1298 (2018).
48. Bjedov, I. & Rallis, C. The target of rapamycin signalling pathway in ageing and lifespan regulation. *Genes (Basel)* **11**, 1043 (2020)
49. Haure-Mirande, J. V. et al. Deficiency of TYROBP, an adapter protein for TREM2 and CR3 receptors, is neuroprotective in a mouse model of early Alzheimer’s pathology. *Acta Neuropathol.* **134**, 769–788 (2017).
50. Hammond, J. W. et al. Complement-dependent synapse loss and microgliosis in a mouse model of multiple sclerosis. *Brain Behav. Immun.* **87**, 739–750 (2020).
51. Bellizzi, M. J., Geathers, J. S., Allan, K. C. & Gelbard, H. A. Platelet-activating factor receptors mediate excitatory postsynaptic hippocampal injury in experimental autoimmune encephalomyelitis. *J. Neurosci.* **36**, 1336–1346 (2016).
52. Fournier, A. P. et al. Single-cell transcriptomics identifies brain endothelium inflammatory networks in experimental autoimmune encephalomyelitis. *Neurol. Neuroimmunol. Neuroinflamm.* **10**, e200046 (2023)
53. Pollak, Y., Ovadia, H., Orion, E., Weidenfeld, J. & Yirmiya, R. The EAE-associated behavioral syndrome: I. Temporal correlation with inflammatory mediators. *J. Neuroimmunol.* **137**, 94–99 (2003).
54. Ucciferri, C. C. et al. Scoring central nervous system inflammation, demyelination, and axon injury in experimental autoimmune encephalomyelitis. *J. Vis. Exp.* <https://doi.org/10.3791/65738> (2024).
55. Yang, H. et al. Mechanisms of mTORC1 activation by RHEB and inhibition by PRAS40. *Nature* **552**, 368–373 (2017).
56. Garami, A. et al. Insulin activation of Rheb, a mediator of mTOR/S6K/4E-BP signaling, is inhibited by TSC1 and 2. *Mol. Cell* **11**, 1457–1466 (2003).
57. Yang, Q., Inoki, K., Kim, E. & Guan, K. L. TSC1/TSC2 and Rheb have different effects on TORC1 and TORC2 activity. *Proc. Natl. Acad. Sci. USA* **103**, 6811–6816 (2006).
58. van Veelen, W., Korsse, S. E., van de Laar, L. & Peppelenbosch, M. P. The long and winding road to rational treatment of cancer associated with LKB1/AMPK/TSC/mTORC1 signaling. *Oncogene* **30**, 2289–2303 (2011).
59. Cai, S. L. et al. Activity of TSC2 is inhibited by AKT-mediated phosphorylation and membrane partitioning. *J. Cell Biol.* **173**, 279–289 (2006).
60. Meyuhas, O. Ribosomal protein S6 phosphorylation: four decades of research. *Int. Rev. Cell Mol. Biol.* **320**, 41–73 (2015).
61. Brandstatter, J. H., Lohrke, S., Morgans, C. W. & Wassle, H. Distributions of two homologous synaptic vesicle proteins, synaptoporin and synaptophysin, in the mammalian retina. *J. Comp. Neurol.* **370**, 1–10 (1996).
62. Koulen, P., Fletcher, E. L., Craven, S. E., Bredt, D. S. & Wassle, H. Immunocytochemical localization of the postsynaptic density protein PSD-95 in the mammalian retina. *J. Neurosci.* **18**, 10136–10149 (1998).
63. Schmitz, F., Konigstorfer, A. & Sudhof, T. C. RIBEYE, a component of synaptic ribbons: a protein’s journey through evolution provides insight into synaptic ribbon function. *Neuron* **28**, 857–872 (2000).
64. Hetz, C. & Saxena, S. ER stress and the unfolded protein response in neurodegeneration. *Nat. Rev. Neurol.* **13**, 477–491 (2017).
65. Errea, O., Moreno, B., Gonzalez-Franquesa, A., Garcia-Roves, P. M. & Villoslada, P. The disruption of mitochondrial axonal transport is an early event in neuroinflammation. *J. Neuroinflamm.* **12**, 152 (2015).
66. van den Berg, R., Hoogenraad, C. C. & Hintzen, R. Q. Axonal transport deficits in multiple sclerosis: spiraling into the abyss. *Acta Neuropathol.* **134**, 1–14 (2017).
67. Mendiola, A. S. et al. Defining blood-induced microglia functions in neurodegeneration through multiomic profiling. *Nat. Immunol.* **24**, 1173–1187 (2023).
68. Zarantonello, A., Revel, M., Grunenwald, A. & Roumenina, L. T. C3-dependent effector functions of complement. *Immunol. Rev.* **313**, 120–138 (2023).
69. Stokowska, A. et al. Complement C3a treatment accelerates recovery after stroke via modulation of astrocyte reactivity and cortical connectivity. *J. Clin. Invest.* **113**, e162253 (2023)

70. Wei, Y. et al. The complement C3-C3aR pathway mediates microglia-astrocyte interaction following status epilepticus. *Glia* **69**, 1155–1169 (2021).
71. Gedam, M. et al. Complement C3aR depletion reverses HIF-1 α -induced metabolic impairment and enhances microglial response to Abeta pathology. *J. Clin. Invest* **113**, e167501 (2023).
72. Reis, E. S., Mastellos, D. C., Hajishengallis, G. & Lambris, J. D. New insights into the immune functions of complement. *Nat. Rev. Immunol.* **19**, 503–516 (2019).
73. Liszewski, M. K. et al. Intracellular complement activation sustains T cell homeostasis and mediates effector differentiation. *Immunity* **39**, 1143–1157 (2013).
74. West, E. E., Kolev, M. & Kemper, C. Complement and the regulation of T Cell responses. *Annu Rev. Immunol.* **36**, 309–338 (2018).
75. Bruggenthies, J. B. et al. A cell-based chemical-genetic screen for amino acid stress response inhibitors reveals torin reverse stress kinase GCN2 signaling. *J. Biol. Chem.* **298**, 102629 (2022).
76. Villa-Gonzalez, M. et al. Pharmacological inhibition of mTORC1 reduces neural death and damage volume after MCAO by modulating microglial reactivity. *Biol. Direct* **19**, 26 (2024).
77. Goldshmit, Y. et al. Rapamycin increases neuronal survival, reduces inflammation and astrocyte proliferation after spinal cord injury. *Mol. Cell Neurosci.* **68**, 82–91 (2015).
78. Huang, K. C. et al. Autophagy disruption reduces mTORC1 activation leading to retinal ganglion cell neurodegeneration associated with glaucoma. *bioRxiv* <https://doi.org/10.1101/2023.01.04.522687> (2023).
79. Vakrakou, A. G. et al. The mTOR signaling pathway in multiple sclerosis; from animal models to human data. *Int. J. Mol. Sci.* **23**, 8077 (2022).
80. Chen, Y. et al. Sephin1, which prolongs the integrated stress response, is a promising therapeutic for multiple sclerosis. *Brain* **142**, 344–361 (2019).
81. Way, S. W. & Popko, B. Harnessing the integrated stress response for the treatment of multiple sclerosis. *Lancet Neurol.* **15**, 434–443 (2016).
82. Zhang, J. et al. LysM-positive neurons drive Tuberous Sclerosis Complex (TSC)-associated brain lesions. *Cell Signal* **100**, 110468 (2022).
83. Wang, J. et al. Wild-type microglia do not reverse pathology in mouse models of Rett syndrome. *Nature* **521**, E1–E4 (2015).
84. Zhou, W. et al. Macrophages from C3-deficient mice have impaired potency to stimulate alloreactive T cells. *Blood* **107**, 2461–2469 (2006).
85. Nguyen, H. X., Galvan, M. D. & Anderson, A. J. Characterization of early and terminal complement proteins associated with polymorphonuclear leukocytes in vitro and in vivo after spinal cord injury. *J. Neuroinflamm.* **5**, 26 (2008).
86. Gaya da Costa, M. et al. Age and sex-associated changes of complement activity and complement levels in a healthy caucasian population. *Front Immunol.* **9**, 2664 (2018).
87. Kotimaa, J. et al. Sex matters: systemic complement activity of female C57BL/6J and BALB/cJ mice is limited by serum terminal pathway components. *Mol. Immunol.* **76**, 13–21 (2016).
88. Tassoni, A. et al. The astrocyte transcriptome in EAE optic neuritis shows complement activation and reveals a sex difference in astrocytic C3 expression. *Sci. Rep.* **9**, 10010 (2019).
89. Rossi, S. et al. Subclinical central inflammation is risk for RIS and CIS conversion to MS. *Mult. Scler.* **21**, 1443–1452 (2015).
90. Kim, B. J., Mastellos, D. C., Li, Y., Dunaief, J. L. & Lambris, J. D. Targeting complement components C3 and C5 for the retina: Key concepts and lingering questions. *Prog. Retin Eye Res.* **83**, 100936 (2021).
91. Biarnes, M. et al. Methodological appraisal of phase 3 clinical trials in geographic atrophy. *Biomedicines.* **11**, 1548 (2023).
92. Liao, D. S. et al. Complement C3 inhibitor pegcetacoplan for geographic atrophy secondary to age-related macular degeneration: a randomized phase 2 trial. *Ophthalmology* **127**, 186–195 (2020).
93. Nguyen, J. V. et al. Myelination transition zone astrocytes are constitutively phagocytic and have synuclein dependent reactivity in glaucoma. *Proc. Natl Acad. Sci. USA* **108**, 1176–1181 (2011).
94. Marsh, S. E. et al. Dissection of artifactual and confounding glial signatures by single-cell sequencing of mouse and human brain. *Nat. Neurosci.* **25**, 306–316 (2022).
95. Cunningham, F. et al. Ensembl 2022. *Nucleic Acids Res.* **50**, D988–D995 (2022).
96. Hao, Y. et al. Integrated analysis of multimodal single-cell data. *Cell* **184**, 3573–3587 e3529 (2021).
97. McCarthy, D. J., Campbell, K. R., Lun, A. T. & Wills, Q. F. Scater: pre-processing, quality control, normalization and visualization of single-cell RNA-seq data in R. *Bioinformatics* **33**, 1179–1186 (2017).
98. Amezcua, R. A. et al. Orchestrating single-cell analysis with bioconductor. *Nat. Methods* **17**, 137–145 (2020).
99. Lun, A. T., McCarthy, D. J. & Marioni, J. C. A step-by-step workflow for low-level analysis of single-cell RNA-seq data with bioconductor. *F1000Res* **5**, 2122 (2016).
100. Germain, P. L., Lun, A., Garcia Meixide, C., Macnair, W. & Robinson, M. D. Doublet identification in single-cell sequencing data using scDblFinder. *F1000Res* **10**, 979 (2021).
101. Marsh, S. E. samuel-marsh/scCustomize: version 1.1.3 (v1.1.3). *Zenodo*. <https://doi.org/10.5281/zenodo.5706430> (2023).
102. Robinson, M. D., McCarthy, D. J. & Smyth, G. K. edgeR: a bioconductor package for differential expression analysis of digital gene expression data. *Bioinformatics* **26**, 139–140 (2010).
103. Ahlmann-Eltze, C. & Huber, W. glmGamPoi: fitting gamma-poisson generalized linear models on single cell count data. *Bioinformatics* **36**, 5701–5702 (2021).
104. Butler, A., Hoffman, P., Smibert, P., Papalexi, E. & Satija, R. Integrating single-cell transcriptomic data across different conditions, technologies, and species. *Nat. Biotechnol.* **36**, 411–420 (2018).
105. Mootha, V. K. et al. PGC-1 α -responsive genes involved in oxidative phosphorylation are coordinately downregulated in human diabetes. *Nat. Genet.* **34**, 267–273 (2003).
106. Subramanian, A. et al. Gene set enrichment analysis: a knowledge-based approach for interpreting genome-wide expression profiles. *Proc. Natl Acad. Sci. USA* **102**, 15545–15550 (2005).

Acknowledgements

The authors wish to thank: Byung-Jin Kim for their assistance with IHC. The authors wish to thank Linda Orzolek and Tyler Creamer at the Johns Hopkins Single Cell and Transcriptomics Core for their assistance with scRNA-seq library generation and sequencing. The authors wish to thank Xiaoling Zhang at the Johns Hopkins Ross Flow Cytometry Core and Ada Tam at the Sidney Kimmel Comprehensive Cancer Center High Parameter Flow Core for assistance with cell sorting. We would also like to acknowledge Dr. Frank Schmitz for providing the 2D9 clone against the Ribeye protein. Funding for this work was provided by the Intramural Research Program of NINDS, NIH T32 GM136577, NIH R01NS041435, NMSS RG-1907-34756, the Fishman Foundation, and the Sol Goldman Charitable Trust. We acknowledge the NIH High-End Instrumentation grant (S10OD021844) for support of the mass spectrometer.

Author contributions

T.G., M.D.S., and P.A.C. planned the experiments. T.G. and M.D.S. performed and analyzed the transcriptomic experiments. T.G. designed the proteomics experiments. S.O., C-H.N., performed and analyzed the proteomics experiments. T.G., A.K., and M.G. performed and analyzed the immunohistochemical experiments. P.A.C. obtained funding for this study. D.J.Z. designed, obtained funding for, and analyzed the γ Synuclein RGC quantification. T.G. designed all figures. T.G. and M.D.S. wrote the manuscript with input from P.A.C. M.A. and D.S.R. provided input regarding experimental design and interpretation as well as discussion and edits during preparation of the manuscript.

Competing interests

The authors declare no competing interests.

Additional information

Supplementary information The online version contains supplementary material available at <https://doi.org/10.1038/s41467-025-58708-3>.

Correspondence and requests for materials should be addressed to Peter A. Calabresi.

Peer review information *Nature Communications* thanks Francesca Gilli and the other anonymous reviewer(s) for their contribution to the peer review of this work. A peer review file is available.

Reprints and permissions information is available at <http://www.nature.com/reprints>

Publisher's note Springer Nature remains neutral with regard to jurisdictional claims in published maps and institutional affiliations.

Open Access This article is licensed under a Creative Commons Attribution-NonCommercial-NoDerivatives 4.0 International License, which permits any non-commercial use, sharing, distribution and reproduction in any medium or format, as long as you give appropriate credit to the original author(s) and the source, provide a link to the Creative Commons licence, and indicate if you modified the licensed material. You do not have permission under this licence to share adapted material derived from this article or parts of it. The images or other third party material in this article are included in the article's Creative Commons licence, unless indicated otherwise in a credit line to the material. If material is not included in the article's Creative Commons licence and your intended use is not permitted by statutory regulation or exceeds the permitted use, you will need to obtain permission directly from the copyright holder. To view a copy of this licence, visit <http://creativecommons.org/licenses/by-nc-nd/4.0/>.

© The Author(s) 2025